

Nature of the low velocity zone in Cascadia from receiver function waveform inversion

by

Ralf T. J. Hansen

B.Sc., The University of Pretoria, 2006

B.Sc. (Hons), The University of Witwatersrand, 2007

A THESIS SUBMITTED IN PARTIAL FULFILLMENT OF
THE REQUIREMENTS FOR THE DEGREE OF

MASTER OF SCIENCE

in

The Faculty of Graduate Studies

(Earth and Ocean Sciences)

THE UNIVERSITY OF BRITISH COLUMBIA

(Vancouver)

October 2011

© Ralf T. J. Hansen 2011

Abstract

Dipping low-velocity zones (LVZs) are a ubiquitous structural element of subduction zones worldwide. In this study we map seismic attributes characterizing the LVZ beneath the Cascadia subduction zone from northern Vancouver Island to northern California using receiver function waveform inversion. Throughout this region, the LVZ is characterized by high V_P/V_S ratios (mean=2.77), strong S -velocity contrasts ($\sim 50\%$) and thicknesses averaging 3.38 km. The LVZ is immediately underlain by a second, weaker layer exhibiting moderate V_P/V_S ratios (mean=1.85) with mean thickness of 4.62 km. We interpret the combined structure in terms of subducting oceanic crust, based on classical structural/petrological descriptions and constraints from previous studies of ophiolites and ocean drill cores. The LVZ is identified with pervasively hydrated, high porosity pillow basalts and sheeted dikes of Layer 2 with possible contributions from sediments (Layer 1). Fluids released from metamorphic dehydration reactions are maintained near lithosphere fluid pressures through an impermeable plate boundary above, and a low porosity, gabbroic/mafic-cumulate dominated Layer 3 below.

Preface

This thesis conforms to the regulations of the Faculty of Graduate Studies.
The content is a minor alteration of a manuscript submitted for publication.
Figures were prepared using Matlab software.

Table of Contents

Abstract	ii
Preface	iii
Table of Contents	iv
List of Tables	vi
List of Figures	vii
Acknowledgements	viii
1 Introduction	1
2 Data Set	6
3 Method	9
3.1 Receiver functions	9
3.2 Inversion of slab attributes	10
4 Results	20
4.1 H_C	20
4.2 R_C	21
4.3 H_{LVZ} and H_{LOC}	25

Table of Contents

4.4	R_{LVZ} and R_{LOC}	26
4.5	$\delta V_S/V_S$	26
4.6	Anisotropy	36
5	Nature of the LVZ	39
6	Conclusions	49
	References	51

List of Tables

- 3.1 Inversion results for station L02A 18

- 4.1 Statistical segment averages of estimates to Figure 4.2 28
- 4.2 Isotropic inversion results for stations used in this study. Also
shown are geographic location, respective networks and total
number of events used for receiver function comparison. 28
- 4.3 Anisotropy estimates for SVI 37

List of Figures

1.1	Tectonic setting and map of Cascadia	2
2.1	Geographic segments and stations	7
2.2	Global event distribution	8
3.1	Ray diagram and receiver functions	11
3.2	Pseudo cross-sections	12
3.3	Inversion steps for station L02A	17
3.4	Select misfit plots for inversion steps (station L02A)	19
4.1	Cascadia contour map	22
4.2	Isotropic model parameter results	23
4.3	Histograms for isotropic model parameter results	24
4.4	Map and histogram for $\delta V_S/V_S$	27
4.5	Anisotropy of SVI	38
5.1	ETS depth distribution	41
5.2	Schematic model for the evolution of oceanic crust	48

Acknowledgements

I would first like to express my gratitude to my supervisor, Michael Bostock. His constant encouragement and support, his insight and thorough knowledge of the field has made this thesis a rewarding and inspirational experience. I would also like to thank Teh-Ru (Alex) Song, and especially Nick Christensen, who provided essential guidance for some of the complex issues in this study. I further want to thank Nick, along with Ron Clowes for serving on my supervisory committee.

My time at UBC was further made memorable by all my fellow graduates who provided much needed distraction from work. I would also express my gratitude to Mark Jellinek who, with his infectious curiosity and open doors, has awakened new fields of interest within me. Being far from home, a special thought goes out to my parents and sisters. With their continuous encouragement and contact, time and distance quickly became insignificant.

Lastly and most importantly, I am eternally grateful for the unending and loving support of my fiancée, Marta. Leaving friends and family to join me in Vancouver, she has been my constant emotional anchor through it all and made enormous sacrifices in the process.

Chapter 1

Introduction

The Cascadia subduction zone is a major component of the tectonic framework along the western coast of North America and extends from northern California to southern British Columbia (Figure 1.1a). The ≤ 10 Ma old Juan de Fuca plate makes up the central part of the subduction system and is bordered by the younger Explorer and Gorda plates to its north and south, respectively. Subduction and/or underthrusting occurs from the Mendocino triple junction at $\sim 40^\circ$ N along the margin up to the Queen Charlotte triple junction near 51° N. The Juan de Fuca plate subducts beneath the North American plate at a rate of ~ 40 mm/a in a northeasterly direction [DeMets et al., 1990], with reduced convergence in the region north of the Nootka fault. Here the Explorer plate undergoes rotation and underthrusts the North American plate [Mazotti et al., 2003], with reduced convergence apparently accommodated by slab stretching in an area evident as shallow swell below northern Vancouver Island [Audet et al., 2008].

Our understanding of subduction zone structure at depth is inferred primarily from seismic observations. In teleseismic tomography studies, the young and relatively warm Juan de Fuca plate is characterized by a positive, quasi-planar, P -wave velocity anomaly of between +2% and +4% evident to ≤ 400 km into the mantle. The northern terminus of this anomaly coincides roughly with the landward projection of the Explorer/Juan de Fuca

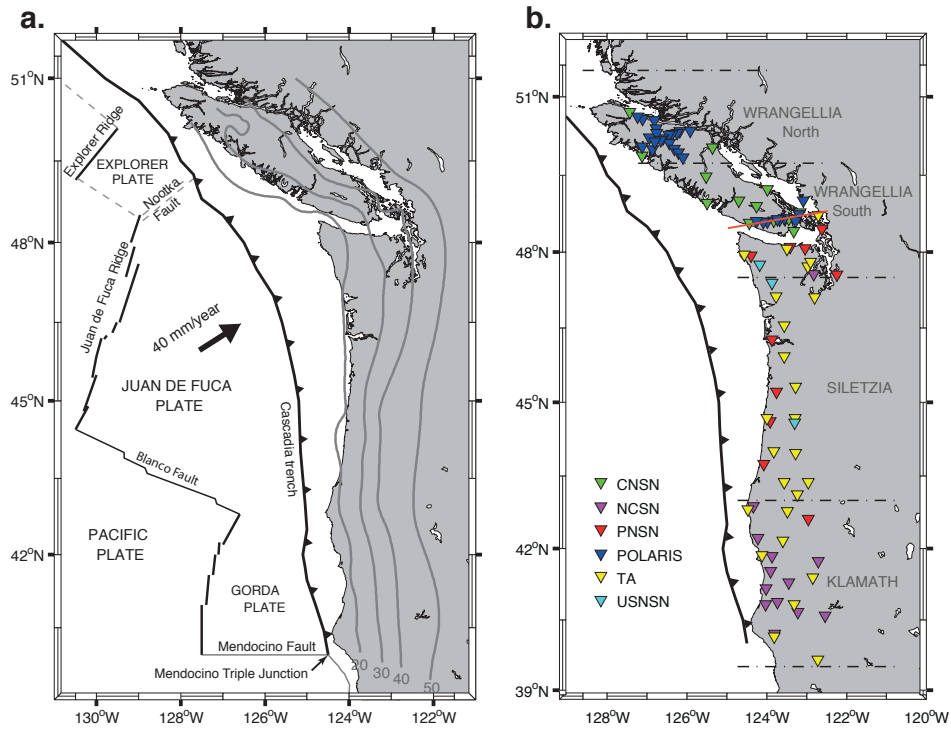


Figure 1.1: (a) Map of the Cascadia subduction zone and its tectonic setting. The contours show the 20, 30, 40, 50 km depth to the top of the plate. (b) Distribution of broadband, three component seismic stations used in this study. Individual networks are represented by different color schemes. Dashed lines indicate the subdivision of the subduction zone into segments as defined by ETS behavior and are labeled after respective geological terranes. The SVI line discussed in section 4 is identified by the red line.

boundary in the direction of the displacement vector [Audet et al., 2008]. Under southern British Columbia, the high-velocity anomaly dips north to northeast at 50° , steepening to $\sim 60^\circ$ [Bostock and Vandecar, 1995; Mercier et al., 2009] beneath northern Washington. The dip shallows once more to between 45° and 60° in southern Washington before returning to angles of $\sim 65^\circ$ below Oregon, where the anomaly weakens substantially ($< 1\%$) [Michealson and Weaver, 1986; Rasmussen and Humphreys, 1988]. More recent studies have confirmed this disruption in structure that points to a fragmented slab and which may be related to previous interactions with the Yellowstone hotspot plume [Burdick et al., 2008; Obrebski et al., 2010; Wagner et al., 2010; Xue and Allen, 2007, 2010]. The velocity anomaly strengthens further south in northern California where it is again evident to ~ 400 km depth with a 50° dip, but disappears abruptly south of the Mendocino triple junction [Burdick et al., 2008; Xue and Allen, 2010].

Shallow (≤ 100 km depth) slab structure is most readily mapped by tracking the distribution of a combined high-reflectivity and low S -wave velocity zone (LVZ) identified in seismic reflection and receiver function studies, respectively. The LVZ, first noted and interpreted as the subducting oceanic crust by Langston [1977,1981] in receiver functions from Corvallis Oregon and Victoria B.C., has since been identified and mapped beneath Vancouver Island, where it is associated with the highly reflective and conductive E-layer [Green et al., 1986; Clowes et al., 1987; Calvert and Clowes, 1990; Kurtz et al., 1990; Cassidy and Ellis, 1993; Nicholson et al., 2005; Soyer and Unsworth, 2006], Washington [Abers et al., 2009] and southern Oregon [Nabelek et al., 1993; Rondenay et al., 2001]. A recent study by Audet et al. [2010] provides evidence for continuity of the LVZ along the entire margin. Their findings confirm the LVZ to be gently dipping and

strongly expressed to depths of ~ 45 km, continuing with a diminishing seismic expression to deeper levels.

Although some studies, in particular those undertaken north of the Canada-US border [Clowes et al., 1987; Calvert et al., 2006], have interpreted the LVZ / E-Layer as residing in the overriding North American plate, a considerable body of the evidence as presented by Nicholson et al [2005] and more recently Audet et al [2010] (see also Abers et al., 2009) favors an interpretation of the LVZ in Cascadia (and in subduction zones globally) as residing in the oceanic plate and, more specifically, the oceanic crust. In this paper, we follow on their interpretations that high V_P/V_S ratios and low V_S characterizing the LVZ at depths < 45 km indicate the presence of overpressured fluids [Christensen, 1984] maintained by an impermeable plate boundary and supplied by prograde metamorphic dehydration reactions. The gradual disappearance of a seismic expression below 45 km depth is inferred to be due to the onset of eclogitization as predicted by thermo-petrological modelling [Peacock and Wang, 1999]. Eclogitization, in turn, compromises the plate boundary seal, causing hydration and serpentinization of the forearc mantle wedge [Bostock et al., 2002; Hyndman and Peacock, 2003].

It has been noted that the downdip limit of Episodic-Tremor-and-Slip (ETS) [Rogers and Dragert, 2003] coincides approximately with the mantle wedge corner, suggesting possible structural controls [Audet et al., 2009; Wada and Wang, 2009]. Moreover, the character of both ETS and regular Wadati-Benioff seismicity are known to vary laterally along the margin. Wadati-Benioff seismicity is sparse in Cascadia and predominantly confined to the region north of the Mendocino triple junction, the Olympic peninsula region and beneath southern Vancouver island, occurring at depths from 30

km to ~ 60 km [Ludwin et al., 1991, Smith and Knapp, 1993]. Variation in timing and frequency of ETS along the Cascadia margin appear to bear a spatial correspondence to the overlying geological terranes of Wrangellia, Siletzia and Klamath [Brudzinski and Allen, 2007]. In addition, a gap in tremor activity and occurrence occurs at 49.5° N in central Vancouver Island [Kao et al., 2009] suggesting a divide in the Wrangellia zone into a northern and southern section.

The revised plate location implicit in the interpretation of the LVZ as oceanic crust or the upper portion thereof [Abers et al., 2009], the spatial association of tremor with high fluid pressures, downdip changes in inferred plate boundary permeability, and geographical variations in ETS, Wadati-Benioff and crustal seismicity [Audet et al., 2010 and references therein] invite a range of questions on structural controls on all styles of seismicity. The purpose of this study is to investigate in detail the physical properties of the LVZ, as well as the subducting and overriding plates by mapping various seismic attributes using scattered teleseismic waves and to examine their relationship with overlying geology and seismicity. Under the assumption that the top of the LVZ represents the plate boundary, we use receiver function inversion to map slab depth, LVZ thickness, V_P/V_S ratios of the overriding continental plate and LVZ, velocity contrast at the plate boundary, and anisotropic fabric internal to the LVZ along the entire Cascadia margin. In addition, we shall characterize structure immediately below the LVZ to shed light on its relation to the subducting plate.

Chapter 2

Data Set

The region of interest in this study encompasses the entire Cascadia forearc region lying between latitudes 39° N to 51° N and longitude 121° W and 130° W. We will divide this area into four subregions of investigation, along the latitude limits set by the ETS studies of Brudzinski and Allen [2007] and Kao et al. [2009]: 49.5° to 52° (Wrangellia North), 47.5° to 49.5° (Wrangellia South) 43° to 47.5° (Siletzia) and 39° to 43° (Klamath), named on the basis of surface geological features (Figure 1.1b).

We have acquired data from 94 broadband, 3-component stations in this region, run by the Canadian National Seismic Network (CNSN), Northern California Seismic Network (NCSN), Pacific Northwest Seismic Network (PNSN) and US National Seismic Network (USNSN). In addition, we have also included stations from temporary networks, notably the USArray Transportable Array (TA) and Portable Lithospheric Analysis and Research Investigating Seismicity (POLARIS-BC) array.

Station coverage (Figure 2.1) is densest along the two POLARIS lines in southern (SVI) and northern (NVI) Vancouver Island and comparatively sparse elsewhere. Events with high signal to noise ratio, magnitudes ≥ 6 and epicentral distances between 30° and 105° were selected for analysis of individual stations. Azimuthal coverage of the resulting event distribution is relatively good, encompassing active margins along most of the Pacific

Chapter 2. Data Set

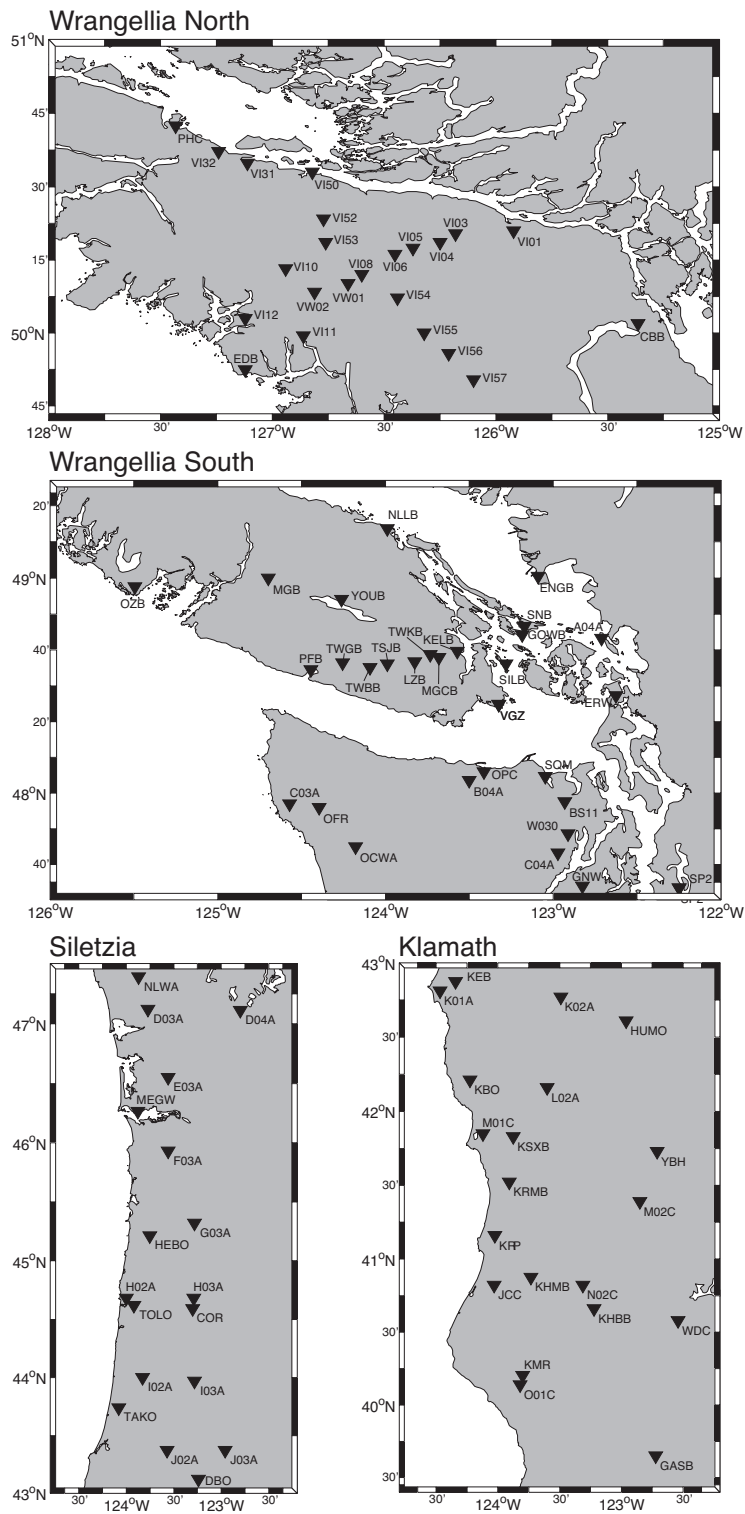


Figure 2.1: Individual station locations and labels for the four segments of the study area.

basin, with poorest coverage over southern and northeastern back azimuths (Figure 2.2).

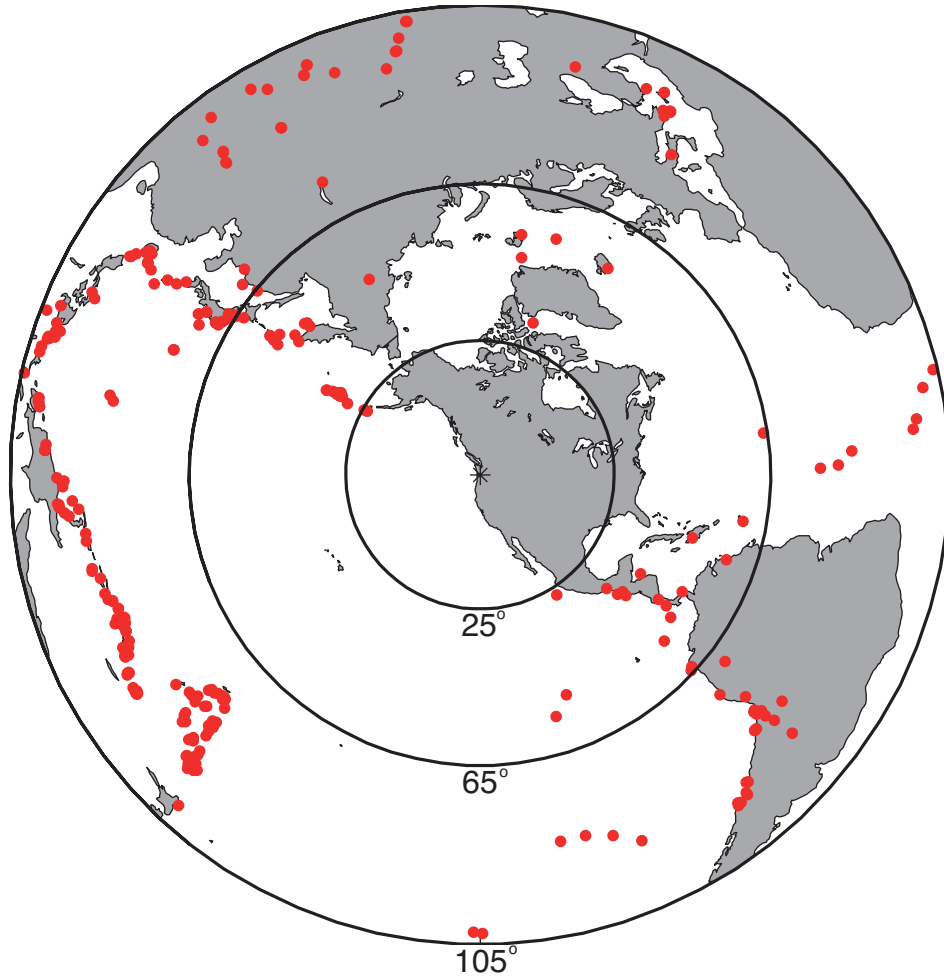


Figure 2.2: Events of magnitude ≥ 6 within 25-105° epicentral distance employed in this study. The region is well covered with the exception of azimuthal sectors northeast and south-southwest.

Chapter 3

Method

3.1 Receiver functions

Individual 3-component seismograms are processed by first rotating the horizontal components into a radial and transverse coordinate system, followed by wavefield decomposition into upgoing P and S_V , S_H components [Bostock, 1998]. The P -wave component, windowed to include the dominant signal, is selected as an estimate of the source-time function. Data are binned according to slowness based on global earthquake location and all seismograms within a given bin are simultaneously deconvolved to produce an estimate of the S_V and S_H components of the Earth's Green function (G_V , G_H) at early times, i.e. receiver functions. Receiver functions are then sorted by back azimuth and band-pass filtered over a frequency band of 0.03 Hz to 0.5 Hz. Assuming that the subducting oceanic plate dominates the teleseismic response in the forearc region, the G_V signature will include 3 sets of oppositely polarized pulses that represent the forward and backscattered P_S , P_{PS} and P_{SS} converted phases (Figure 3.1a), displayed as blue and red coded traces for 2 styles of oceanic crustal model (Figure 3.1b,c). The timing of these scattered phases will depend primarily on integrated P and S velocity structure and their amplitudes are sensitive to contrasts in the stiffness tensor at structural boundaries [Bostock et al., 2001, Audet et

al., 2008]. In an isotropic, laterally homogenous medium the G_H component is zero, so any energy on this component will originate from either lateral heterogeneity or anisotropy.

To facilitate subsequent analysis, we plot receiver functions in order of station distance from the trench to create pseudo-linear profiles representing each of the four subregions in this study (Figure 3.2a). Note that relative distances between stations along profiles are not preserved. The LVZ is clearly evident at times representing 20 to 40 km depth for stations between the coast and the landward limit defined by the forearc valleys associated with the Georgia Strait, Pudget Sound and Willamette Valley. These profiles are useful in identifying the laterally coherent signal associated with the LVZ and allow us to resolve uncertainties related to weak arrivals and ambiguities related to multiple signals in subsequent processing as described below.

3.2 Inversion of slab attributes

We invert the receiver functions for estimates of slab geometry and material properties at individual stations along the Cascadia forearc. We use a total of 740 seismic events with an average of 117 receiver functions for each of the 92 stations, and employ the forward modeling method of Frederiksen and Bostock [2000] in combination with the Neighborhood algorithm of Sambridge [1999] to perform the inversion.

The forward modeling method employs models with planar dipping layers and is computationally economical since it employs a high-frequency approximation. For a given model, travel time and amplitude of a specific phase are determined on a layer-segment by layer-segment basis, using eigen-

3.2. Inversion of slab attributes

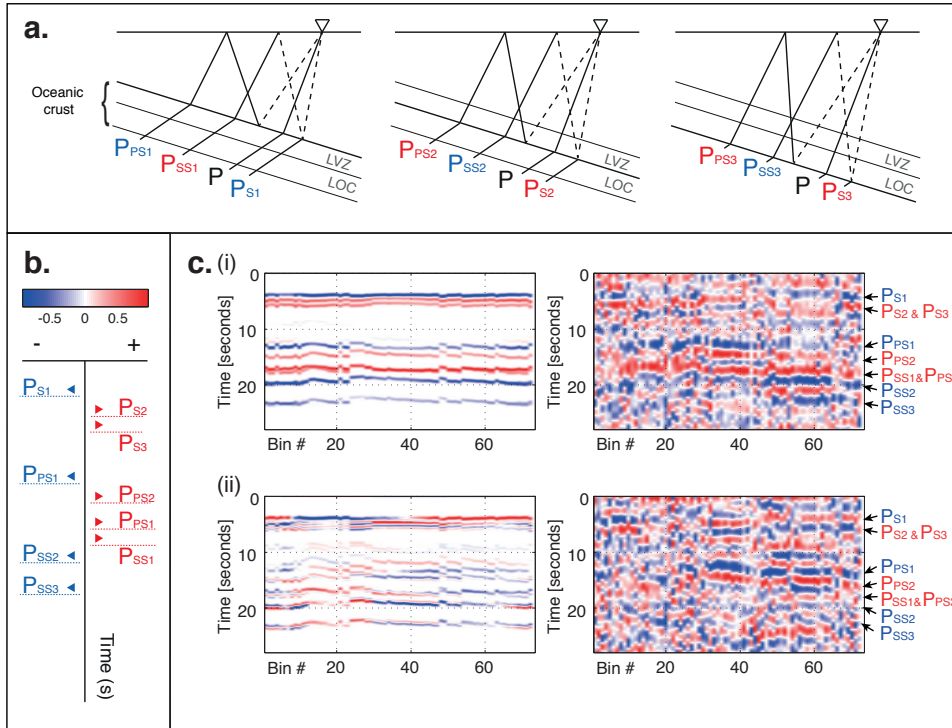


Figure 3.1: (a) Ray diagram showing the P to S converted phases interacting with a dipping LVZ and an additional layer LOC (discussed in detail in a later section later). Schematic receiver functions for the phases in (a) are presented in (b) with positive and negative polarities as red and blue, respectively. Colorbar shows amplitude, scaled relative to P component, for the (c) (i) radial and (ii) transverse components of model inversion results and input receiver functions at station KELB, sorted by back azimuth of incident wavefield. Labels correspond to phases identified in (a).

3.2. Inversion of slab attributes

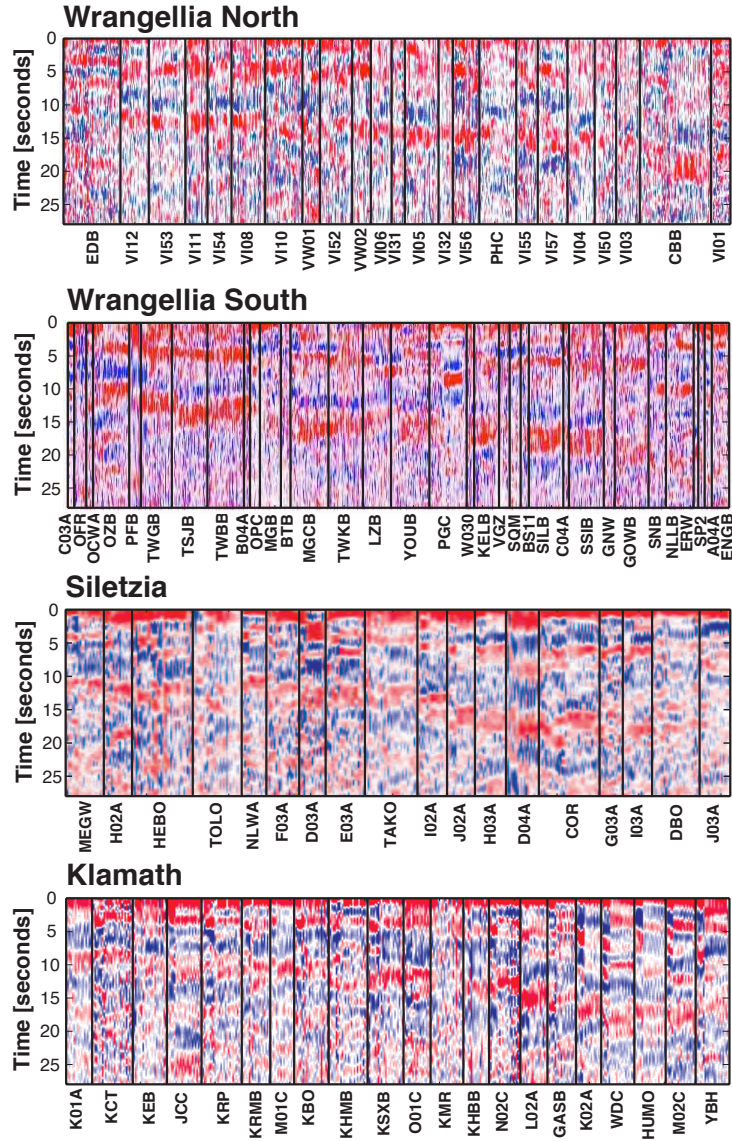


Figure 3.2: Radial component receiver functions for all data sorted by station distance to trench location and combined into pseudo-linear profiles. Vertical lines separate bins assigned to each station, where the width is proportional to the number of events. The plots demonstrate the existence of the LVZ beneath all stations used in this study.

3.2. Inversion of slab attributes

vector decompositions and coordinate system rotations to compute vertical slowness and reflection/transmission coefficients. The Neighborhood algorithm employs the forward modelling method to efficiently sample model space and converge toward the global minimum of a misfit defined using a normalized correlation coefficient based on all seismograms [Frederiksen et al., 2003]:

$$f_c(d_{ijk}, s_{ijk}) = 1 - \frac{\sum_{i=1}^{N_t} \sum_{j=1}^{N_s} \sum_{k=1}^{N_c} w_i^t w_k^c d_{ijk} s_{ijk}}{\sqrt{\sum_{i=1}^{N_t} \sum_{j=1}^{N_s} \sum_{k=1}^{N_c} w_i^t w_k^c d_{ijk}^2} \sqrt{\sum_{i=1}^{N_t} \sum_{j=1}^{N_s} \sum_{k=1}^{N_c} w_i^t w_k^c s_{ijk}^2}}. \quad (3.1)$$

In (3.1), d_{ijk}, s_{ijk} are the data and synthetics, respectively; $i, j, k / N_t, N_s, N_c$ refer to the index/number of traces, samples and components respectively; w_k^c and w_i^t represent weights associated with individual components and traces that can be scaled as desired. An initial set of models is generated, their misfits are calculated using (3.1) and each is assigned a “neighborhood” (Voronoi cell) on the representative misfit surface. The search is driven towards the lowest misfit model by continuously resampling the Voronoi cells for the select group of newly generated models that fall below a defined misfit threshold [Sambridge, 1999]. In this study we apply the Neighborhood algorithm in a layer-stripping procedure wherein we successively introduce greater complexity into our solution through the following steps, presented graphically in Figure 3.3:

1. We first obtain estimates for thickness (H_C) and V_P/V_S ratio of the overriding crust (R_c) using a simplified two-layer isotropic model with a single, planar, dipping interface by modeling only those arrivals associated with the top of the LVZ. All of H_C , R_C , and strike (ϕ_C) and

3.2. Inversion of slab attributes

dip (δ_C) of the dipping interface are permitted to vary within loosely prescribed limits.

2. Next, we consider the first of two structural parameterizations for the subducting plate, namely that it can be represented solely by a single layer, that is, the LVZ underlain by a mantle half-space. We obtain estimates for thickness (H_{LVZ}) and V_P/V_S ratio using a three-layer, isotropic model with planar dipping layers, by modeling arrivals from both top and bottom of the LVZ. The material parameters characterizing the overriding continental crust ($H_C, R_C, \phi_C, \delta_C$) are now more tightly constrained based on results obtained in step 1, whereas $H_{LVZ}, R_{LVZ}, \phi_{LVZ}, \delta_{LVZ}$ are allowed to vary more widely.
3. In the second structural parameterization, we model the subducting oceanic plate with two layers underlain by a mantle half space and search for optimal estimates of thickness (H_{LVZ}, H_{LOC}) V_P/V_S ratios (R_{LVZ}, R_{LOC}) for these two layers using a four-layer, isotropic model with planar dipping layers. Material parameters of the overriding continental crust are tightly constrained based on step 1, whereas $H_{LVZ/LOC}, R_{LVZ/LOC}, \phi_{LVZ/LOC}, \delta_{LVZ/LOC}$ are allowed to vary more widely.
4. Finally, we obtain estimates for anisotropy of the subducting oceanic crust using a four-layer anisotropic model with planar, dipping layers wherein we again model scattered waves from both top and bottom of the oceanic crust. Isotropic structure is now tightly constrained based on results obtained in step 2. Anisotropy of the LVZ is characterized by % magnitude in P and S , trend (ψ) and plunge (θ) assuming hexagonal

3.2. Inversion of slab attributes

symmetry and a constant value of $\eta = \frac{F}{A-2L} = 0.95$, where A , F , L are elastic constants defined in Anderson [1989]. These parameters are permitted to vary within the loosely assigned limits, and estimates of parameters determined from steps 3 are now tightly constrained.

In the early stages of our analysis, we employed only steps 1, 2 and 4. That is, we considered an oceanic plate comprising only LVZ and underlying half-space. In a significant number of instances we found it difficult to converge to a single model in step 2, owing to evidence for the presence of a second, weaker, low-velocity layer underlying the primary LVZ (see e.g. figure 7 in Nicholson et al. [2005]; Abers et al. [2009]) and that we label here LOC (lower oceanic crust). In figure 3.3, we compare the synthetic seismograms corresponding to models determined at the end of each of steps 1, 2, 3 and 4 with actual data from station L02A. This station shows clearly the reverberations associated with the LOC layer.

Each of steps 1–4 involves five inversion runs to a total of 500 iterations, with individual inversion runs initialized with different seeds. As expected, each step is characterized by a decrease in the misfit function defined in (3.1) and progressively tighter limits are imposed on parameters for the next step. Limits are determined from the collection of models that fall within the lower 2% misfit range. Layer thickness estimates are made on the assumption of a constant V_P of 6.5 km/s (based on an average crustal value from the tomography study of Ramachandran et al. [2005]), since travel times of receiver functions for typical data sets are sensitive primarily to V_P/V_S and H/V_P . Although this value may not be fully representative of average crustal P -velocity away from southern Vancouver Island and Puget Sound, it simplifies comparison.

3.2. Inversion of slab attributes

Results of steps (1-4) for station L02A are shown in Figure 3.3 and 3.4, and Table 3.1. Note that there exist two comparable minima for step 2 (Figure 3.4a,b) and corresponding models (Figure 3.3b,c). In this case the profiles in Figure 3.2 provide a framework for constraining or selecting that model that best matches spatial trends. However, the addition of another layer for the oceanic crust, labelled here LOC, in step 3 reconciles the two arrivals within a single model (Figure 3.3d and 3.4c) and produces a further decrease in misfit. Only a single H_{LVZ} minimum is visible in Figure 3.4d.

3.2. Inversion of slab attributes

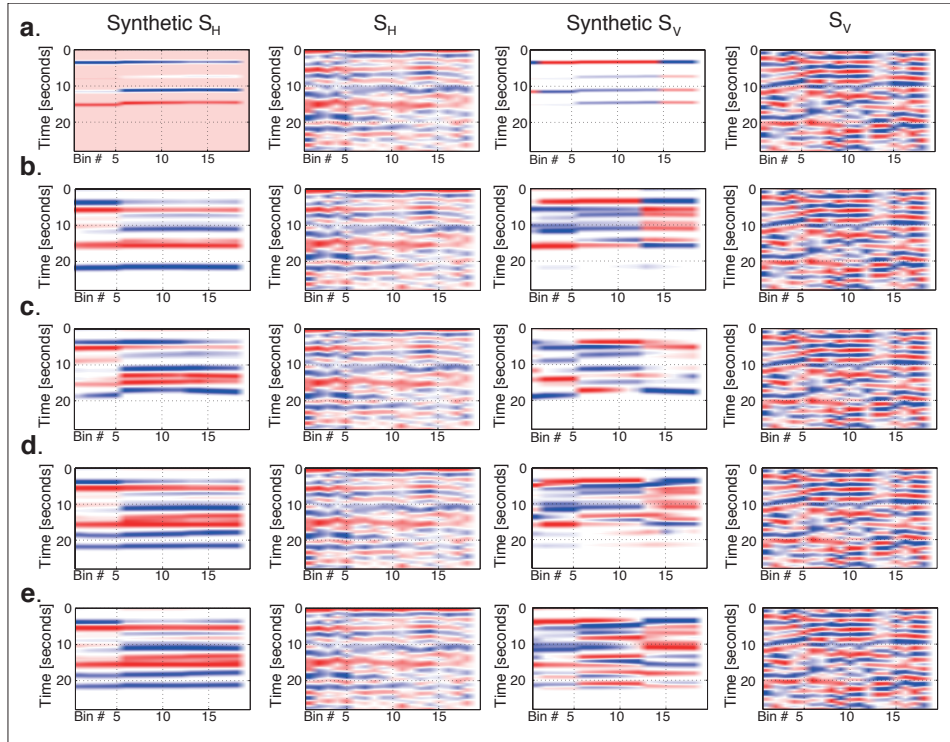


Figure 3.3: Example of inversion steps for station L02A. Columns represent radial and transverse components for both synthetic and real receiver functions. Parameter values employed at each steps can be found in Table 3.1. (a) Results for step 1. One-layer model phases match seismic receiver functions. (b) Results for step 2. Note that the P_{ss} for the 2nd set of arrivals match a signal at $t > 20$. (c) Alternate results for P_{ss} phase arrival in step 2 at $t = 17$. Note a better signal representation for the transverse component. (d) Results for step 3. Both arrivals from (b) and (c) are recovered in the signal. (e) Results for step 4. Note that the transverse component is an improvement to (d).

3.2. Inversion of slab attributes

Table 3.1: Results of inversion steps 1–4 for station L02A.

Start	Min	Best fit	Max
H_C	22	28	32
R_C	1.55	-	2.32
ϕ_C	0	-	360
δ_C	0	-	25
Step 1 (Figure 3.3a)		(Misfit = 0.76796)	
H_C	26.07	28.28	28.71
R_C	1.83	1.86	1.91
Step 2 (Figure 3.3b)		(Misfit = 0.62845)	
H_C	27.74	28.10	28.49
R_C	1.83	1.87	1.89
H_{LVZ}	5.96	6.29	7.39
R_{LVZ}	2.62	2.93	3.11
Step 2 (Figure 3.3c)		(Misfit = 0.61452)	
H_C	26.07	26.09	26.47
R_C	1.94	1.97	2.00
H_{LVZ}	4.31	4.57	5.00
R_{LVZ}	3.13	3.30	3.34
Step 3 (Figure 3.3d)		(Misfit = 0.57048)	
H_C	26.07	26.49	27.13
R_C	1.91	1.95	2.00
H_{LVZ}	2.68	3.29	4.06
R_{LVZ}	2.80	3.23	3.30
H_{LOC}	3.37	4.02	5.32
R_{LOC}	1.91	2.12	2.12
Step 4 (Figure 3.3e)		(Misfit = 0.57104)	
ϕ_C	336.4	359.1	360.0
δ_C	10.1	13.2	14.8
% P_{LVZ}	0.1	0.1	4.6
% S_{LVZ}	0.4	3.9	14.7
ψ_{LVZ}	247.6	352.8	360.0
θ_{LVZ}	3.8	26.6	45.9
ϕ_{LVZ}	10.1	40.8	65.8
δ_{LVZ}	6.6	10.1	12.0
ϕ_{LOC}	319.9	353.6	360.0
δ_{LOC}	2.7	5.6	7.8

3.2. Inversion of slab attributes

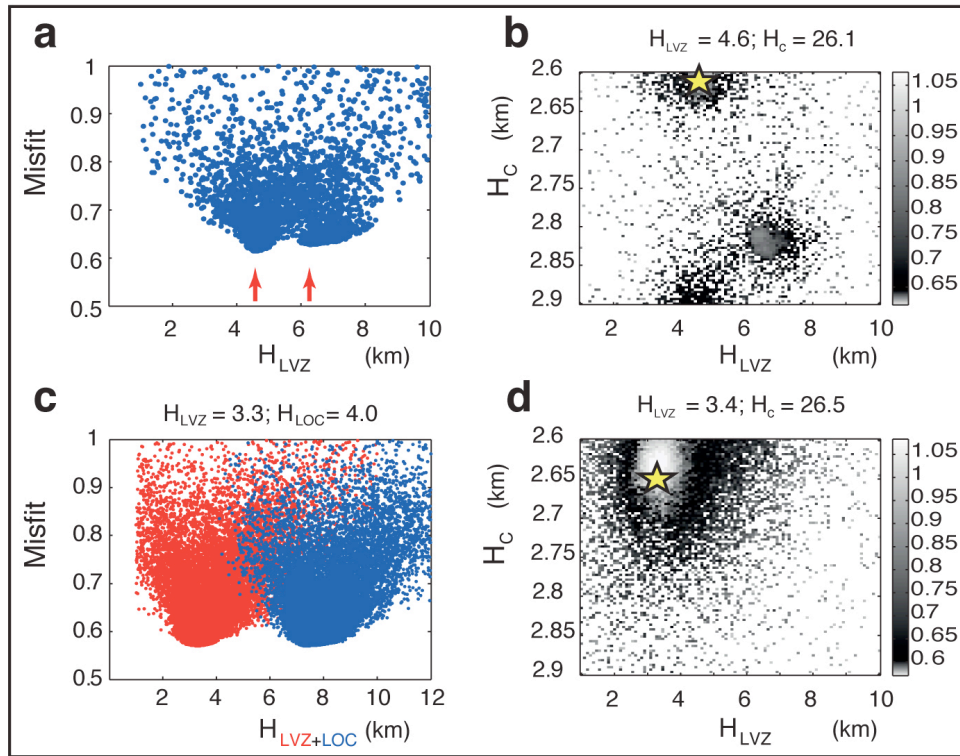


Figure 3.4: Parameter plots from model inversion for station L02A. The yellow star indicates location of the model with lowest misfit. (a) Misfit vs. H_{LVZ} for step 2. Note the two possible models associated with two misfit minima (indicated by red arrows). (b) Slice through the misfit surface along the $H_C - H_{LVZ}$ plane at for step 2. Note the two possible solutions that tie in with two possibilities for H_C . (c) Misfit against H_{LVZ} and H_{LOC} (step 3). (d) Slice through the misfit surface along the $H_C - H_{LVZ}$ plane for step 3. We now observe convergence to a single model misfit minimum.

Chapter 4

Results

In the following subsections we summarize the model inversion results. For each attribute H_C , R_C , $H_{LVZ/LOC}$, $R_{LVZ/LOC}$, $\delta V_S/V_S$, we provide maps displaying geographic variation along the margin and histograms for each of the four ETS segments as well as the entire data set (see also Tables 4.1-4.3).

4.1 H_C

We begin with the depth to plate boundary that, in the area of interest, corresponds to H_C , the thickness of the continental crust (Figure 4.1). Variations in this quantity are visualized by plotting depth contours computed using a minimum curvature algorithm from the GMT mapping tools [Wessel and Smith, 1991]. Given the diminished signal of the LVZ at depths greater than ~ 45 km, only contours for 20, 30 and 40 km are shown. Contours are generated using a gridding technique and are reliable only where constrained by nearby stations. Recall that our depth estimates assume an average P -velocity of 6.5 km/s for the continental crust across the region and therefore some of the variability represented within the contours may be due to unmodelled velocity structure. Depth estimates differ by an average ± 3.3 km from the model of Audet et al. [2010] and are most significant in northern Wrangellia between 50° N - 51° N, and between $\sim 40^\circ$ to 41° N in

the Klamath segment. In both these regions the present model predicts a shallower subducting plate.

4.2 R_C

The V_P/V_S ratio of the overriding continental crust, R_C (Figure 4.2d) ranges from 1.55 to 2.32 with an average of 1.80 ± 0.19 (sample mean \pm standard deviation) over the entire margin. The distribution of R_C on histogram (Figure 4.3b) is positively skewed for Cascadia as a whole, reaching a maximum at $R_C = 1.7$.

Little systematic variation is evident in the geographic distribution of R_C . Northern Wrangellia has an average R_C of 1.71 ± 0.16 with a localized region of relatively high values evident in the area of postulated slab stretching [Audet et al., 2008]. Note in particular R_C values of 1.87 and 1.89 for stations VI53 and VW01, respectively, that contrast with the mean of 1.66 ± 0.08 for remaining stations. Higher R_C values are observed in Wrangellia South and Siletzia, 1.83 ± 0.15 and 1.89 ± 0.21 , respectively. Average R_C estimates for Klamath are found to be lower at 1.75 ± 0.19 . Stations of highest R_C can be found straddling the 40 km contour as well as the periphery of the subduction zone margin in the north and south (stations PHC, CBB, SP2, G03A, O01C). These measurements may be influenced by the locations near the edge of the boundary of subducting oceanic crust, or by the loss of signal in close proximity to the mantle wedge.

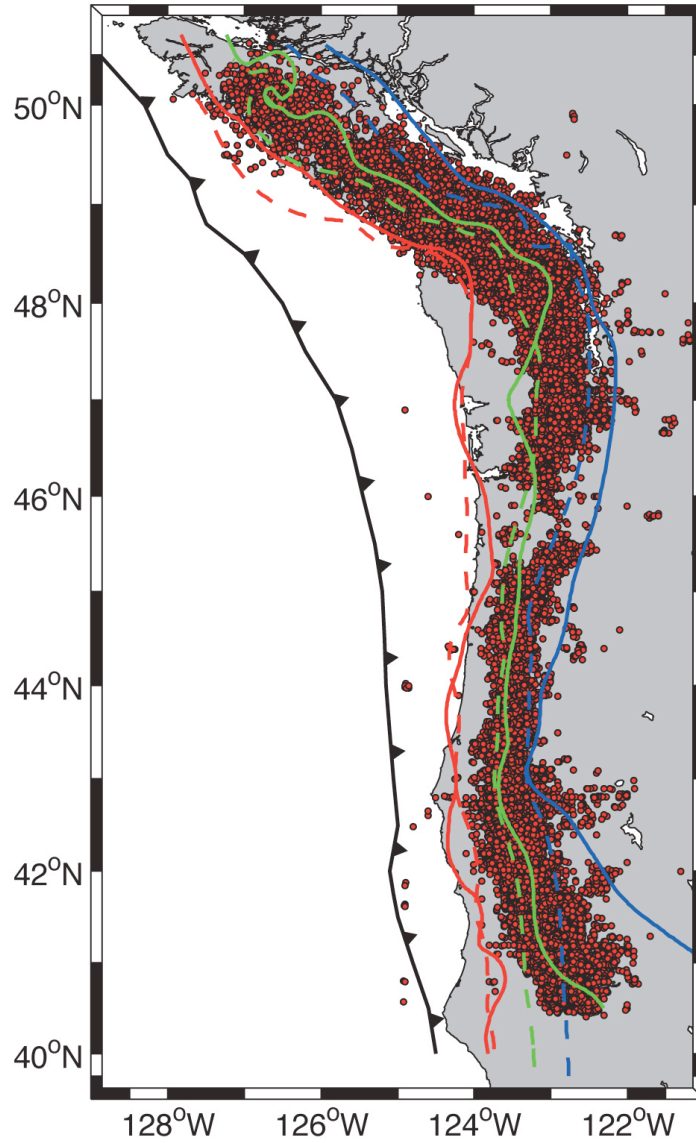


Figure 4.1: Plate model showing 20 km (red), 30 km (green) and 40 km (blue) depth contours in solid lines, plotted over ETS epicentral locations along the Cascadia margin. Dashed lines show plate contours from Audet et al. [2010].

4.2. R_C

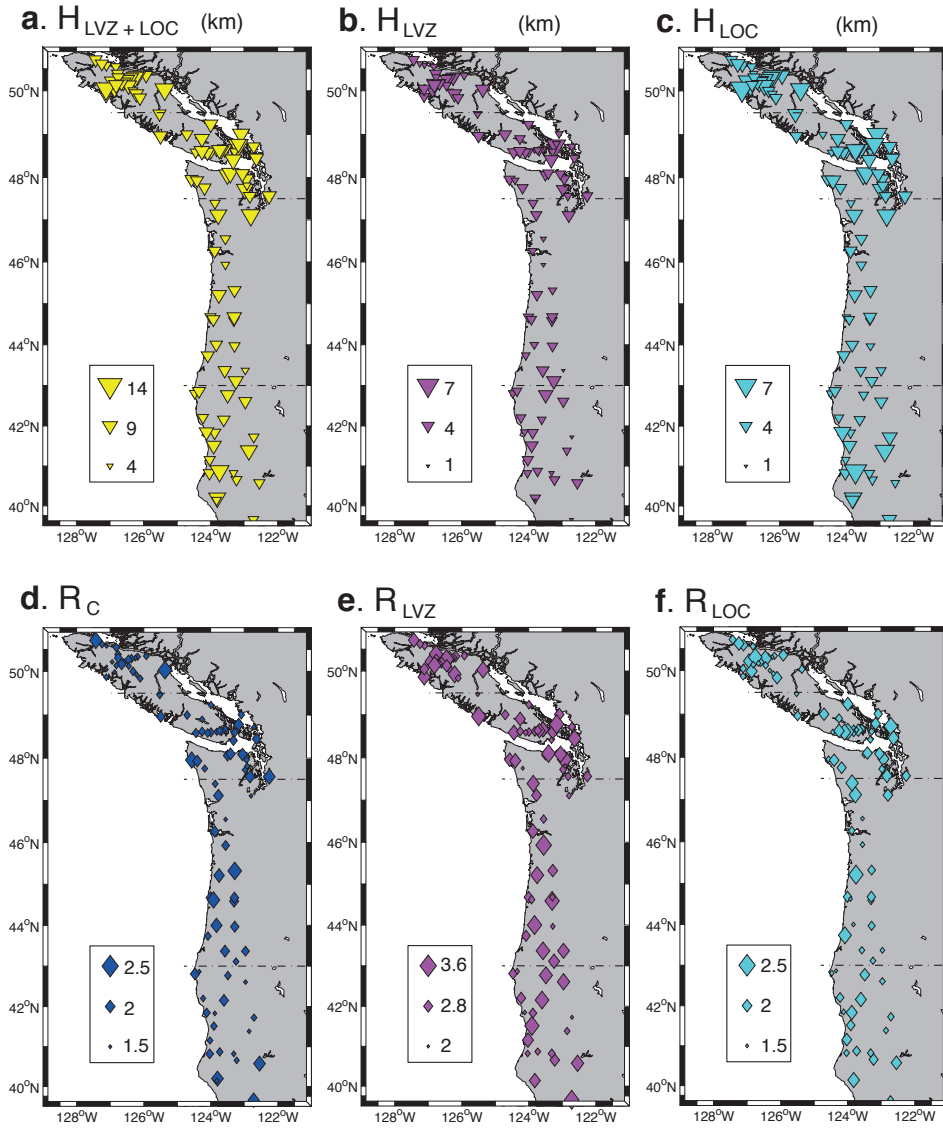


Figure 4.2: Results of modeling for parameters (a) H_C , (b) H_{LVZ} , (c) H_{LOC} , (d) R_C , (e) R_{LVZ} and (f) R_{LOC} shown for stations at their geographic locations. Size represents a relative measure of parameter magnitude.

4.2. R_C

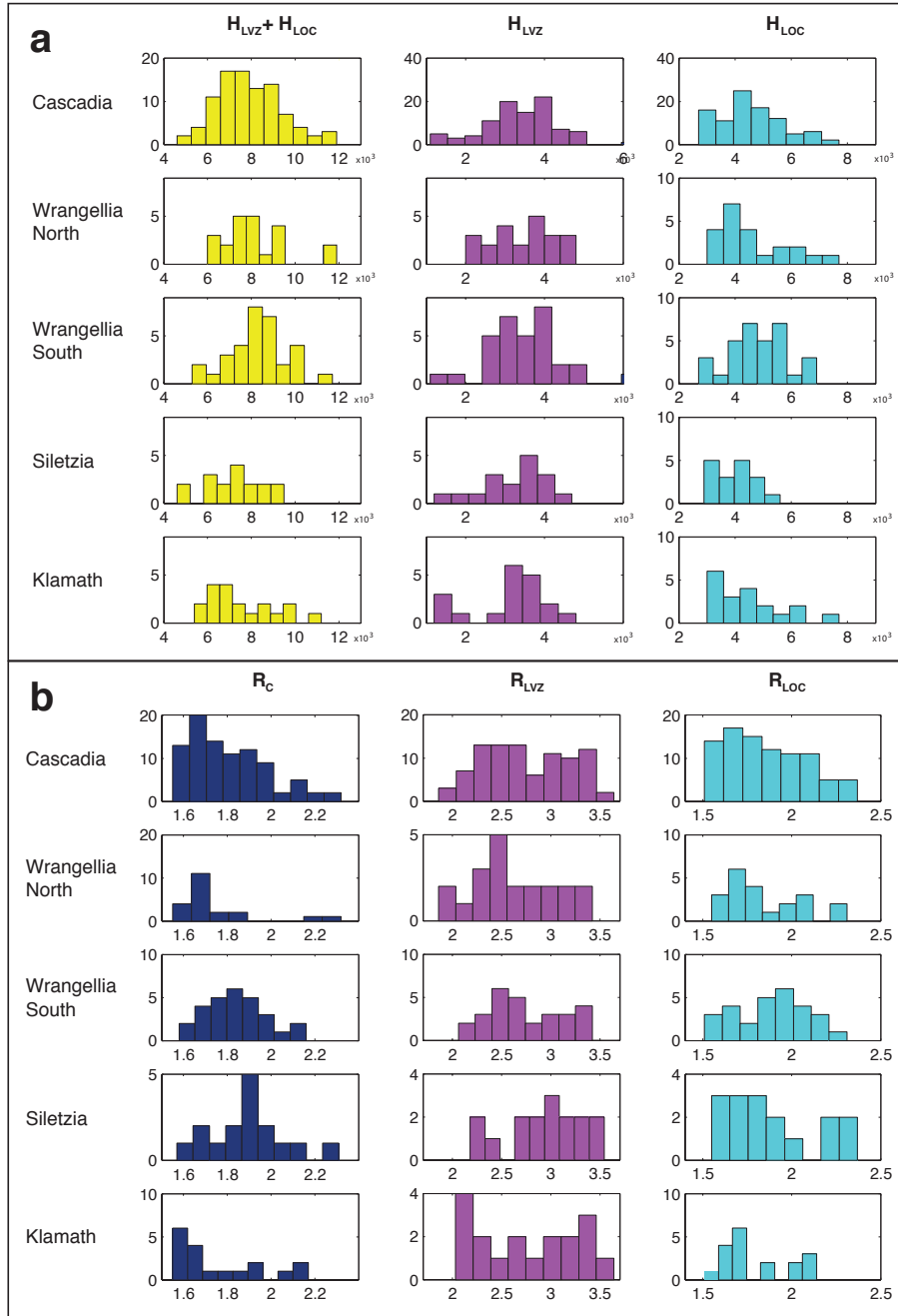


Figure 4.3: (a) Parameter results for thickness H_{LVZ} , H_{LOC} , and the sum of both, shown as a histogram for geographic segments used in this study. Similarly, (b) shows results for V_P/V_S ratios R_C , R_{LVZ} and R_{LOC} . Means and standard deviations for (a) and (b) can be found in Table 4.1. 24

4.3 H_{LVZ} and H_{LOC}

As explained earlier, we have parametrized the oceanic plate as 2 layers of variable thickness (and V_P/V_S ratio) underlain by a mantle half-space. The top layer corresponds to the LVZ, and its thickness H_{LVZ} (Figure 4.2b) ranges from 1 km to 6.6 km with a mean of 3.38 ± 0.94 km for the entire margin. Moreover, the four individual geographic segments all display comparable values: Wrangellia North (3.52 ± 0.87 km), Wrangellia South (3.47 ± 0.96 km), Siletzia (3.28 ± 0.94 km) and Klamath (3.24 ± 0.92 km) (Figure 4.3c).

Estimates for the thickness of the second layer, H_{LOC} , (Figure 4.2c) average 4.62 ± 1.22 km for a range of 2.8 to 8 km across Cascadia. Once again we find there is little systematic variation in H_{LOC} and segment estimates (Figure 4.3c) for Wrangellia North (4.58 ± 1.30 km), Wrangellia South (4.85 ± 1.05 km), Siletzia (4.19 ± 0.94 km) and Klamath (4.60 ± 1.51 km) are comparable.

The combined thickness of the two layers $H_{LVZ} + H_{LOC}$ (Figures 4.2,3a) averages 8.00 ± 1.58 km, ranging from 4 to 12 km with little geographic trend evident in the variation. Mean values for Wrangellia North and South are slightly larger (8.09 ± 1.46 km and 8.32 ± 1.39 km, respectively) than those obtained for Siletzia (7.48 ± 1.53 km) and Klamath (7.85 ± 1.70 km). Note that thickness estimates have been corrected for an average slab dip of 15° so as to represent the true (versus vertical) thickness of the layers.

4.4 R_{LVZ} and R_{LOC}

V_P/V_S ratios of the two layers within the oceanic plate differ significantly and are $R_{LVZ}=2.77 \pm 0.41$ (Figure 4.2e) and $R_{LOC}=1.85 \pm 0.22$ (Figure 4.2f). Little systematic variation in either parameter is evident along the margin, where R_{LVZ} segment averages are: Wrangellia North (2.71 ± 0.38), Wrangellia South (2.79 ± 0.39), Siletzia (2.85 ± 0.43) and Klamath (2.65 ± 0.44). Averages for R_{LOC} are: Wrangellia North (1.84 ± 0.23), Wrangellia South (1.90 ± 0.19), Siletzia (1.84 ± 0.27) and Klamath (1.84 ± 0.21).

4.5 $\delta V_S/V_S$

The amplitudes of forward and back scattered waves both depend upon $\delta V_S/V_S = 2 \frac{(V_2 - V_1)}{(V_1 + V_2)}$, the S -wave velocity contrast at the scattering interface (reverberations also possess some sensitivity to density contrast). This sensitivity enables us to estimate $\delta V_S/V_S$ at the inferred plate boundary, that is, the top of the LVZ. This quantity averages -0.45 ± 0.13 within a range of -0.15 to -0.73 (Figure 4.4b) with the following segment averages: Wrangellia North (-0.46 ± 0.13), Wrangellia South (-0.44 ± 0.13) Siletzia (-0.44 ± 0.13) and Klamath (-0.45 ± 0.15). High values can be found in the area from $\sim 42^\circ$ N to 44° N, 48.5° N and near $\sim 50^\circ$ N (Figure 4.4a).

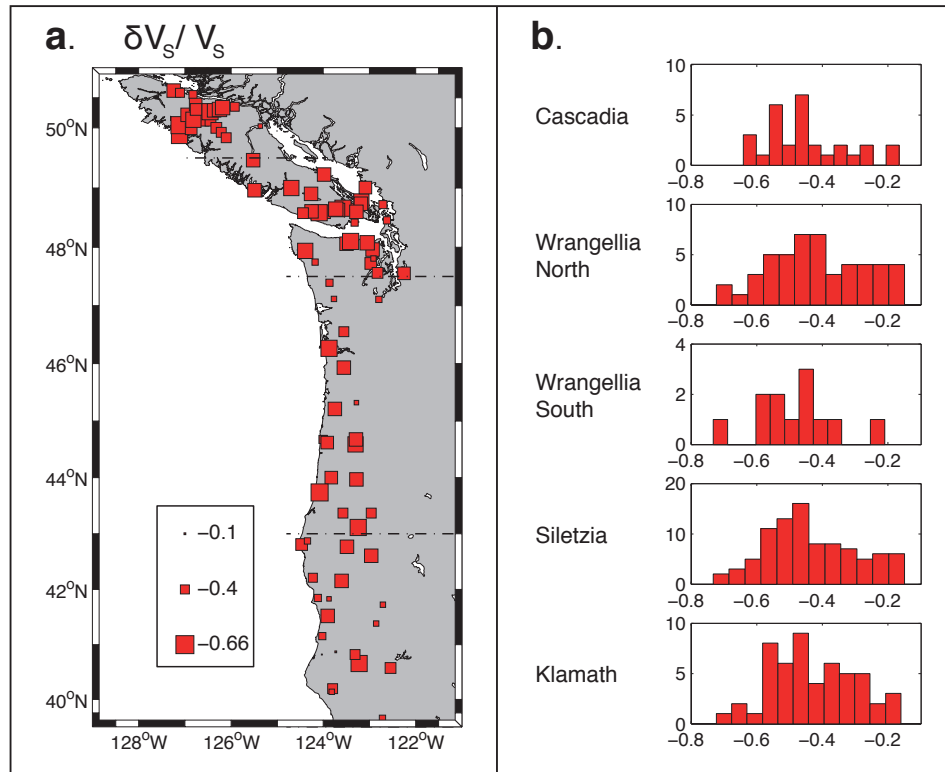


Figure 4.4: Results for reflectivity ($\delta V_S/V_S$) of the interface between overriding continental crust and subducting oceanic crust. (a) Symbols represent individual stations at their geographic locations. Symbols are scaled by magnitude. (b) $\delta V_S/V_S$ segment histograms.

Table 4.1: Isotropic means and standard deviations of determined seismic attributes. H values are given in km.

Segment	$H_{LVZ} + H_{LOC}$	H_{LVZ}	H_{LOC}	R_C	R_{LVZ}	R_{LOC}
Cascadia	8.00 ± 1.54	3.38 ± 0.94	4.62 ± 1.22	1.80 ± 0.19	2.77 ± 0.41	1.85 ± 0.22
Wrangellia N.	8.09 ± 1.46	3.52 ± 0.87	4.58 ± 1.30	1.71 ± 0.16	2.71 ± 0.38	1.84 ± 0.23
Wrangellia S.	8.32 ± 1.39	3.47 ± 0.96	4.85 ± 1.05	1.83 ± 0.15	2.79 ± 0.39	1.90 ± 0.19
Siletzia	7.48 ± 1.53	3.28 ± 0.94	4.19 ± 0.94	1.89 ± 0.21	2.85 ± 0.43	1.84 ± 0.27
Klamath	7.85 ± 1.70	3.24 ± 0.92	4.60 ± 1.51	1.75 ± 0.19	2.65 ± 0.44	1.84 ± 0.21

Table 4.2: Isotropic inversion results for stations used in this study. Also shown are geographic location, respective networks and total number of events used for receiver function comparison.

Station	Lon	Lat	Net	Events	H_C	R_C	H_{LVZ}	R_{LVZ}	H_{LOC}	R_{LOC}	$\delta V_S/V_S$
A04A	-122.71	48.72	TA	90	43.46	1.58	2.89	2.55	4.83	2.31	-0.47
B04A	-123.50	48.06	TA	69	26.90	1.88	3.85	2.60	5.79	1.64	-0.32
BS11	-122.93	47.96	XU	84	34.21	1.68	3.84	3.42	4.94	2.12	-0.68
Continued on next page											

Table 4.2 – continued from previous page

Station	Lon	Lat	Net	Events	H_C	R_C	H_{LVZ}	R_{LVZ}	H_{LOC}	R_{LOC}	$\delta V_S/V_S$
BTB	-125.52	49.47	CN	231	31.02	1.77	2.80	2.14	5.36	1.59	-0.19
C03A	-124.57	47.95	TA	62	16.92	2.21	3.88	2.95	3.97	1.63	-0.45
C04A	-122.97	47.72	TA	63	33.78	1.71	4.38	2.55	5.66	1.75	-0.39
CBB	-125.36	50.03	CN	391	35.93	2.32	4.82	3.18	6.77	1.75	-0.31
COR	-123.30	44.59	IU	189	32.26	1.94	3.53	3.38	2.90	1.74	-0.54
D03A	-123.77	47.12	TA	75	28.00	2.00	3.86	2.82	5.65	2.20	-0.34
D04A	-122.80	47.11	TA	73	34.43	1.55	4.34	2.30	6.46	2.02	-0.39
DBO	-123.24	43.12	UO	186	41.87	1.67	4.73	3.03	4.20	1.68	-0.58
E03A	-123.56	46.55	TA	110	27.75	1.55	2.15	2.41	4.14	1.56	-0.43
EDB	-127.12	49.87	CN	140	19.62	1.63	3.68	3.16	3.09	1.67	-0.64
ENGB	-123.09	49.01	BC	89	42.42	1.77	2.67	2.83	6.91	1.92	-0.46
ERW	-122.63	48.45	UW	32	40.14	1.89	3.34	3.24	5.20	2.09	-0.53
F03A	-123.56	45.93	TA	97	23.97	1.84	1.71	3.54	3.52	1.61	-0.61
G03A	-123.28	45.32	TA	41	33.33	2.31	2.84	2.82	4.51	1.83	-0.20
Continued on next page											

4.5. $\delta V_S/V_S$

Table 4.2 – continued from previous page

Station	Lon	Lat	Net	Events	H_C	R_C	H_{LVZ}	R_{LVZ}	H_{LOC}	R_{LOC}	$\delta V_S/V_S$
GASB	-122.72	39.65	BK	62	28.76	2.10	1.35	3.41	4.78	1.68	-0.48
GNW	-122.83	47.56	UW	142	35.99	2.00	3.16	2.46	4.22	2.08	-0.21
GOWB	-123.18	48.74	BC	226	37.08	1.76	6.43	2.72	5.30	1.78	-0.43
H02A	-124.00	44.68	TA	57	20.69	1.96	3.71	2.73	2.97	1.91	-0.33
H03A	-123.29	44.68	TA	63	33.04	1.90	3.85	2.34	4.57	1.92	-0.36
HEBO	-123.75	45.21	UW	174	20.04	2.07	3.83	3.21	4.81	2.37	-0.53
HUMO	-122.96	42.61	BK	78	38.01	1.56	3.79	3.15	4.28	1.70	-0.73
I02A	-123.83	44.00	TA	61	25.04	2.10	2.75	3.42	4.40	1.55	-0.48
I03A	-123.28	43.97	TA	59	37.29	1.89	3.70	2.18	2.97	1.82	-0.28
J02A	-123.57	43.37	TA	59	29.63	1.93	4.16	3.31	3.88	1.68	-0.52
J03A	-122.96	43.37	TA	52	43.94	1.85	1.22	3.06	3.36	1.58	-0.51
JCC	-124.03	40.82	BK	74	17.31	1.83	3.09	2.26	3.99	1.69	-0.20
K01A	-124.47	42.81	TA	58	17.28	1.94	3.22	2.71	2.98	1.61	-0.33
K02A	-123.49	42.77	TA	47	33.17	1.72	4.92	3.21	3.47	2.03	-0.60
Continued on next page											

4.5. $\delta V_S/V_S$

Table 4.2 – continued from previous page

Station	Lon	Lat	Net	Events	H_C	R_C	H_{LVZ}	R_{LVZ}	H_{LOC}	R_{LOC}	$\delta V_S/V_S$
KBO	-124.23	42.21	NC	73	21.99	1.66	3.31	2.75	3.24	1.86	-0.49
KEB	-124.34	42.87	BK	84	18.18	1.56	3.34	2.17	4.18	1.51	-0.47
KELB	-123.57	48.66	BC	146	32.01	1.76	2.90	3.05	5.58	1.82	-0.53
KHBB	-123.22	40.66	NC	63	25.13	1.67	3.54	2.83	3.28	1.52	-0.52
KHMB	-123.73	40.87	NC	92	18.10	1.73	3.45	2.34	7.68	1.84	-0.30
KRMB	-123.91	41.52	NC	65	19.87	1.74	4.33	3.39	4.73	1.89	-0.64
KRP	-124.02	41.16	NC	90	19.37	1.68	3.87	2.97	2.99	2.03	-0.55
KSXB	-123.88	41.83	NC	86	20.94	1.55	3.85	2.58	3.38	2.12	-0.56
L02A	-123.60	42.16	TA	54	26.49	1.95	3.29	3.23	4.02	2.11	-0.49
LZB	-123.82	48.61	CN	302	25.96	1.68	1.69	2.62	4.12	1.93	-0.44
M01C	-124.12	41.85	TA	49	20.26	1.80	2.60	2.13	5.86	1.61	-0.17
M02C	-122.85	41.39	TA	66	35.93	1.55	3.16	2.35	6.52	1.64	-0.41
MEGW	-123.88	46.27	UW	105	21.25	1.89	2.81	3.02	4.65	1.76	-0.46
MGB	-124.70	49.00	CN	214	28.07	1.76	4.31	2.61	2.94	2.00	-0.39
Continued on next page											

4.5. $\delta V_S/V_S$

Table 4.2 – continued from previous page

Station	Lon	Lat	Net	Events	H_C	R_C	H_{LVZ}	R_{LVZ}	H_{LOC}	R_{LOC}	$\delta V_S/V_S$
MGCB	-123.68	48.63	BC	264	28.68	1.79	3.30	2.98	5.44	2.00	-0.50
N02C	-123.31	40.82	TA	69	24.51	1.58	1.91	2.52	3.54	1.74	-0.36
NLLB	-123.99	49.23	CN	302	40.82	1.68	3.70	2.45	4.66	2.08	-0.56
NLWA	-123.87	47.39	US	31	22.46	1.70	3.31	3.14	3.01	2.23	-0.60
O01C	-123.82	40.14	TA	59	20.58	1.58	1.23	2.96	4.73	2.14	-0.43
OCWA	-124.18	47.75	US	52	18.69	1.68	3.81	2.06	4.12	1.96	-0.26
OFR	-124.40	47.93	UW	182	15.64	1.96	2.49	2.97	5.26	1.98	-0.41
OPC	-123.41	48.10	UW	142	23.79	1.94	3.76	3.29	6.52	2.00	-0.54
OZB	-125.49	48.96	CN	231	21.54	1.92	4.14	3.42	4.26	1.86	-0.53
PFB	-124.44	48.58	CN	182	20.51	1.82	4.09	3.10	2.75	1.59	-0.52
PHC	-127.43	50.71	CN	207	26.91	2.23	3.88	2.96	4.16	1.78	-0.42
SILB	-123.28	48.60	BC	246	34.57	1.82	3.02	2.89	3.01	1.70	-0.53
SNB	-123.17	48.78	CN	227	38.66	1.99	2.64	3.40	6.47	1.99	-0.53
SP2	-122.25	47.56	UW	97	39.52	2.16	3.75	2.66	4.83	1.91	-0.21
Continued on next page											

4.5. $\delta V_S/V_S$

Table 4.2 – continued from previous page

Station	Lon	Lat	Net	Events	H_C	R_C	H_{LVZ}	R_{LVZ}	H_{LOC}	R_{LOC}	$\delta V_S/V_S$
SQM	-123.05	48.08	UW	158	28.31	2.02	3.68	3.18	4.74	1.99	-0.45
SSIB	123.39	48.76	BC	258	36.67	1.90	2.60	2.77	5.48	1.85	-0.56
TAKO	-124.08	43.74	UW	157	25.98	1.76	3.16	2.69	4.49	2.29	-0.59
TOLO	-123.92	44.62	UW	141	23.40	2.19	3.70	2.45	3.71	1.56	-0.26
TSJB	-123.99	48.60	BC	243	24.37	1.80	3.40	2.41	4.07	2.20	-0.47
TWBB	-124.09	48.58	BC	262	22.84	1.75	3.72	2.29	4.50	2.20	-0.38
TWGB	-124.26	48.61	BC	172	22.47	1.78	4.11	2.63	5.09	2.05	-0.39
TWKB	-123.73	48.64	BC	250	27.14	1.74	2.82	2.63	6.31	1.57	-0.58
VGZ	-123.32	48.41	CN	336	29.15	1.86	4.78	2.31	5.41	1.71	-0.21
VI01	-125.92	50.35	VI	34	37.62	1.69	2.75	2.45	5.39	1.93	-0.37
VI03	-126.18	50.34	VI	49	37.17	1.67	3.31	2.66	6.20	1.67	-0.46
VI04	-126.25	50.31	VI	59	34.11	1.58	4.74	2.51	6.04	1.55	-0.45
VI05	-126.37	50.29	VI	72	28.24	1.72	4.46	3.02	4.11	1.81	-0.55
VI06	-126.45	50.27	VI	47	27.00	1.81	4.08	3.42	3.08	2.22	-0.62
Continued on next page											

4.5. $\delta V_S/V_S$

Table 4.2 – continued from previous page

Station	Lon	Lat	Net	Events	H_C	R_C	H_{LVZ}	R_{LVZ}	H_{LOC}	R_{LOC}	$\delta V_S/V_S$
VI08	-126.60	50.20	VI	103	26.42	1.72	3.15	2.71	5.79	1.81	-0.44
VI10	-126.94	50.22	VI	93	29.14	1.55	2.36	2.92	6.34	2.12	-0.61
VI11	-126.86	49.99	VI	50	26.62	1.55	3.78	2.32	3.06	2.12	-0.40
VI12	-127.12	50.05	VI	68	25.77	1.55	4.17	2.74	7.72	1.74	-0.56
VI31	-127.11	50.58	VI	24	30.85	1.56	2.14	2.45	4.14	1.96	-0.44
VI32	-127.24	50.62	VI	25	29.10	1.68	2.27	2.49	5.09	2.08	-0.39
VI50	-126.82	50.55	VI	39	32.31	1.75	2.72	2.04	3.56	1.71	-0.15
VI52	-126.77	50.39	VI	80	27.89	1.72	4.10	3.30	3.16	1.71	-0.63
VI53	-126.76	50.31	VI	95	25.68	1.87	3.13	2.33	4.06	2.32	-0.47
VI54	-126.44	50.12	VI	54	29.49	1.64	3.38	2.84	6.06	1.71	-0.54
VI55	-126.32	50.00	VI	40	32.77	1.73	1.98	2.55	4.04	1.55	-0.38
VI56	-126.21	49.93	VI	52	31.84	1.61	4.76	3.24	3.47	1.61	-0.64
VI57	-126.10	49.84	VI	60	27.02	1.69	3.72	2.33	4.20	2.03	-0.32
VW01	-126.66	50.17	VI	45	31.57	1.89	3.97	2.37	3.79	1.60	-0.25
Continued on next page											

4.5. $\delta V_S/V_S$

Table 4.2 – continued from previous page

Station	Lon	Lat	Net	Events	H_C	R_C	H_{LVZ}	R_{LVZ}	H_{LOC}	R_{LOC}	$\delta V_S/V_S$
VW02	-126.81	50.14	VI	40	27.87	1.63	4.80	3.24	4.20	1.66	-0.60
W030	-122.91	47.81	XG	79	34.90	1.65	1.07	2.10	4.19	1.51	-0.16
WDC	-122.54	40.58	BK	77	29.14	2.17	3.75	3.13	3.14	2.05	-0.46
YBH	-122.71	41.73	BK	76	35.14	1.68	1.45	2.06	4.96	1.73	-0.21
YOUB	-124.26	48.90	CN	268	32.33	1.66	3.53	2.93	5.15	1.81	-0.55

4.6 Anisotropy

In Figure 4.5 we present results pertaining to anisotropy of the LVZ, as determined for SVI stations in Wrangellia South (see also Table 4.2). These stations are characterized by large quantities of high quality data, enabling analysis of anisotropy, whereas we are less confident of results at other locations. We assume hexagonal symmetry (Figure 4.5a), and plot the symmetry axis as the horizontal projection of a constant length vector (in red). Variations in trend (ψ) and plunge (θ) of the symmetry axis are indicated by yellow triangular sectors with narrower sectors representing more tightly constrained axis trends. Symmetry axis orientations fall predominantly to the northeast. Inversion runs for four stations (GOWB, MGCB, SSIB, LZB) resulted in two comparable minima, the second indicated in Figure 4.5a as dashed lines. Plunge (θ) varies from 4.1° - 74.5° , with an average of 23.6° . Values for the magnitude of S -wave anisotropy (Figure 4.5b) range from 0.3 to 29.7% with a mean of 15.4%. Figure 4.5c shows P -wave anisotropy magnitude ranging between 2.5 to 24.8%, with an average of 8.9%.

Table 4.3: Anisotropy estimates for the LVZ (SVI stations). Solution multiples are indicated by numbered subscripts. $\theta_{corrected}$ is the dip of the plate interface for the fast symmetry axis, corrected for an average dip of 15° . $\phi_{average}$ represents the combined average strike for the top and bottom interfaces of the LVZ.

Station	Lon	Lat	% <i>P</i> -wave	% <i>S</i> -wave	ψ	θ	$\theta_{corrected}$	$\phi_{average}$
GOWB ₁	-123.18	48.74	9.5	11.2	350.2	78.5	63.5	114.8
GOWB ₂	-123.18	48.74	7.7	25.2	39.3	52.0	37.0	150.7
KELB	-123.57	48.66	6.1	16.9	30.7	35.7	20.7	127.9
LZB ₁	-123.82	48.61	3.3	26.6	98.1	89.5	74.5	353.5
LZB ₂	-123.82	48.61	15.7	20.4	274.7	60.8	45.8	168.3
MGCB ₁	-123.68	48.63	2.5	16.4	194.5	24.5	9.5	120.0
MGCB ₂	-123.68	48.63	2.6	24.5	28.3	29.9	14.9	138.4
PFB	-124.44	48.58	24.8	2.3	14.2	26.7	16.7	358.7
SILB	-123.28	48.60	7.1	4.3	53.5	19.1	4.1	122.9
SNB ₁	-123.17	48.78	3.8	0.3	171.3	56.1	41.1	105.8
SNB ₂	-123.17	48.78	6.9	29.8	35.1	22.9	7.9	101.8
SSIB	-123.39	48.76	3.4	9.2	204.4	47.9	32.9	101.8
TSJB	-123.99	48.60	7.7	12.5	31.7	23.5	13.5	95.2
TWBB	-124.09	48.58	7.1	20.4	3.8	21.2	11.2	128.7
TWGB	-124.26	48.61	9.3	18.2	20.8	15.7	5.7	118.0
TWKB	-123.73	48.64	18.4	26.0	2.7	29.5	14.5	341.1

4.6. Anisotropy

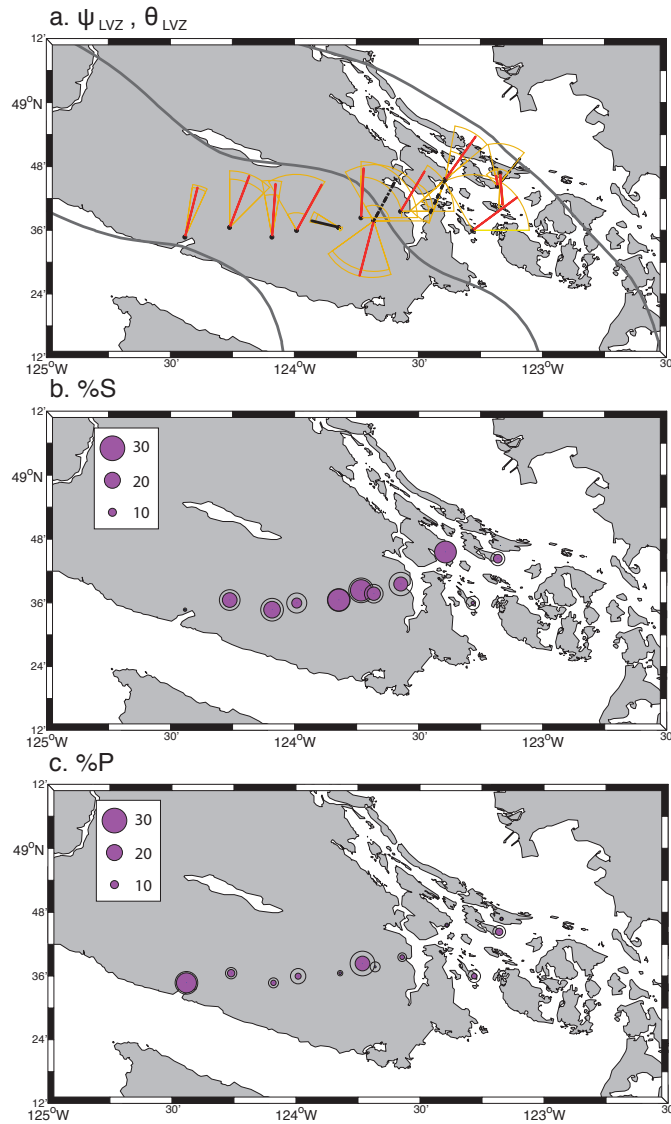


Figure 4.5: Anisotropy estimates for stations along the SVI array. (a) Red line segments represent surface projection of a constant length vector that indicates the orientation of the symmetry axis. Longer/shorter segments are more shallowly/steeply dipping axes. Yellow arcs define limits on dip determined from the best 2% model results (step 4). Plate contours at 20, 30, 40 km depths are shown as dark gray lines (b) Magnitude of S-wave anisotropy at individual stations. Colored circles represent the best model result and larger concentric circles show the upper limit of the 2% best models. (c) Magnitude of P-wave anisotropy as for (b).

Chapter 5

Nature of the LVZ

In the previous sections, we have compiled information on a series of seismic attributes that characterize the Cascadia subduction zone. Average R_C values can be loosely correlated with the geology of the overlying crust. Wrangellia North is characterized by a variety of volcanic, plutonic (quartz diorites), sedimentary and metamorphic rocks in an island arc setting [Muller, 1977]. The corresponding V_P/V_S of 1.71 ± 0.16 falls slightly below that for arc lithologies (1.77) and average continental crust (1.76) [Christensen, 1996]. The larger R_C values for Wrangellia South and Siletzia (1.83 ± 0.15 , 1.89 ± 0.21 , respectively) may be representative of a predominantly basaltic rock matrix ($V_P/V_S = 1.89$) that would be expected for the accreted oceanic crustal terranes found in these areas [Trehu et al., 1994]. Along the Klamath segment, the geology is again dominated by arc crust [Fuis et al., 1987; Oldow et al., 1989] and the average R_C of 1.75 ± 0.19 is consistent with the value of 1.77 measured for sample arc rocks in a laboratory setting. Although there is a correlation between average measured R_C for the margin segments and values expected on the basis of surface geology, we caution that variations in R_C across individual stations, as expressed within quoted errors, are large. With the added exception of the depth to top of plate, H_C , it is difficult to discern any significant, larger-scale geographic variation in any of the remaining attributes that would allow us to further address the

causes responsible for the segmentation of tremor along Cascadia [Brudzinski and Allen, 2007]. Nevertheless, there are a number of other important conclusions that can be drawn from the results as we outline below.

We have modelled continental crust in the Cascadia forearc as a homogeneous, isotropic layer, the depth of which corresponds to the plate boundary or LVZ. Our model for plate boundary depth, shown in Figure 4.1, is similar to that of Audet et al [2010] but differs slightly at the northern end within Wrangellia North and at the southern end of the Klamath segment. In both regions, our model indicates a more shallowly subducting plate that may be related to the presence of slab edges. Our model also differs from Audet et al. [2010] near 47°N where a seaward verging divot appears in the 20 and 30 km depth contours. This feature occurs in an area where station density is low and as such is due primarily to station D04A.

Following Audet et al. [2010], we use the geometry of slab contours to consider the importance of structural controls on ETS by plotting contours on a map of epicentral distribution. By identifying each epicenter with a depth determined from the slab contours, we may plot the depth distribution of tremor locations on histograms (see also Kao et al. [2005]). Assuming that tremor location is controlled by a depth dependent process, the viability of a given depth model can be assessed by the width of the histogram distribution. Epicentral information was obtained from Kao et al. [2009] for the Vancouver Island region (Wrangellia North and the northern portion of Wrangellia South) and from the interactive tremor map on the PNSN website (www.pnsn.org/tremor/; Wech, A. G., 2010) for other regions. ETS depth locations are determined using bi-linear interpolation of depth contours for a given slab model, for example that in Figure 4.1. Comparable histograms for the plate models of McCrory et al. [2006], Audet et al [2010]

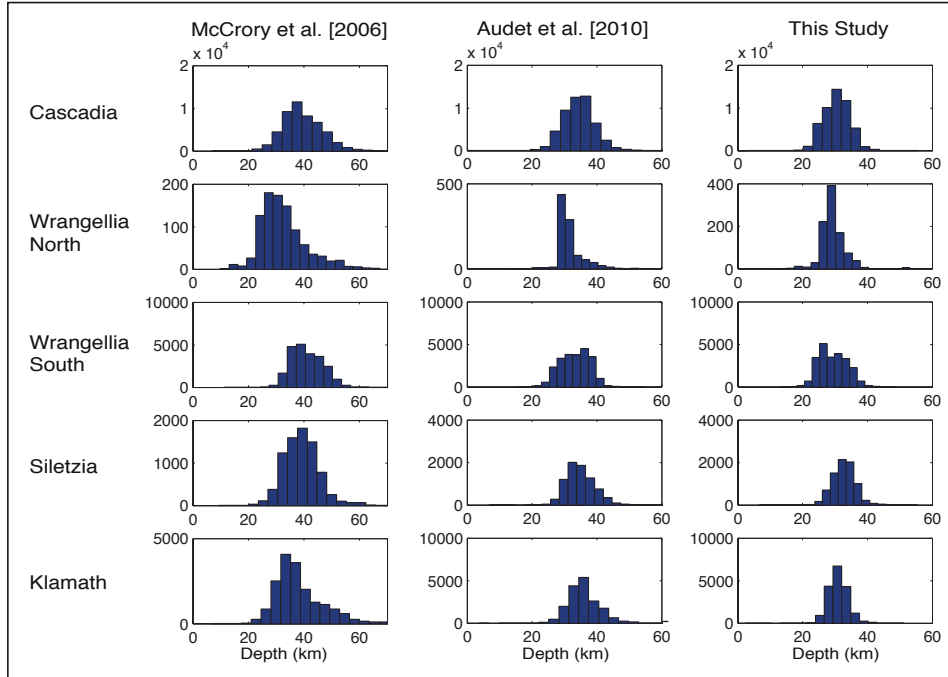


Figure 5.1: Histogram of ETS depths determined from slab contours of McCrory et al. [2006], Audet et al. [2010] and this study.

and this study are shown in Figure 5.1. It should be noted that a different ETS data set was employed in Audet et al. [2010] so there need not be an exact correspondence between the histograms presented here and in that study.

Our model achieves the most symmetric distribution of ETS events for all segments. Fixing V_P at 6.5 km/s will undoubtedly introduce some artificial variation within the depth contours, but the tight depth window of 20-41 km for all segments and a consistent modal maximum at near 30 km nevertheless favours a mechanism for ETS that is depth controlled. Direct comparison between models reveals significant disagreement between this

study and McCrory et al. [2006] (± 8 km), and to a lesser extent with Audet et al. [2010] (± 3 km). The concentration in ETS depths associated with plate models based on mapping of the LVZ, lends increased confidence to the association of this structure with the top of the downgoing plate.

An important contribution of this study concerns the characterization and interpretation of the LVZ. In some previous studies (e.g. Langston [1981], Rondenay et al. [2001], Nicholson et al. [2005], Audet et al. [2009, 2010]) this feature had been identified with the subducting oceanic crust in its entirety. This identification naturally followed from the time separation between scattered phases from the top and bottom of the LVZ that was broadly consistent with typical oceanic crustal thicknesses when transformed using generic 1-D velocity models. However, by closely examining differential delay times of both forward and back scattered waves, Audet et al. [2009] used a variant of the Zhu and Kanamori [2000] stacking technique to demonstrate that the LVZ below southern Vancouver Island is actually marked by extreme V_P/V_S ratios ($R_{LVZ} = 2.35$) and also by smaller thicknesses ($H_{LVZ} = 4.6$ km) than typical of oceanic crust.

In this study, we have employed detailed waveform modelling to demonstrate that comparable values hold for the LVZ along the entire Cascadia margin (mean $R_{LVZ} = 2.77$, $H_{LVZ} = 3.38$ km). Moreover, waveform modelling has indicated that structure at the top of the subducting plate is better represented by a sequence of 2 layers, namely the LVZ and an underlying layer, labeled LOC, with reduced V_P/V_S ($R_{LOC} = 1.85$) and a mean thickness $H_{LOC} = 4.62$ km. The combined thickness of the two layers $H_{LVZ} + H_{LOC}$ (8.0 ± 1.54) falls close to that expected of typical oceanic crust. The identification of this 2-layer (LVZ+LOC) package with oceanic crust can be further rationalized as follows.

It has long been noted that crustal structure across ocean basins possesses a relatively simple layered structure that has been conventionally divided into 3 layers. Layer 1 is composed of sediments of variable thickness (0.5-3 km) and low V_P (1.7-2.0 km/s). Layer 2 comprises pillow basalts ($V_P= 3.2-5$ km/s) and sheeted dykes ($V_P=6.5$ km/s), 2 ± 1 km thick with porosity of 20% and 5-10%, respectively (Layer 2 permeability 10^{-12} to 10^{-11} m²). Layer 3 comprises the remaining oceanic crust including gabbro ($V_P = 6.7 - 6.9$ m/s, 2-4% porosity) grading to layered gabbro and ultramafics (negligible porosity) down to the Moho [Salisbury et al., 1989; Fisher, 1998].

Analysis of ophiolitic sections [Salisbury and Christensen, 1978, Salisbury et al., 1989] and *in situ* velocities [Rohr, 1994] reveals that hydration and retrograde metamorphism (prehnite-pumpellyite through greenschist to amphibolite facies) occurs primarily in the upper part of the oceanic crust, implying that water circulation is pervasive throughout Layers 1 and 2 within the young plate, but is far more restricted within Layer 3.

In situ borehole investigations [Fisher et al., 1997; Fisher, 1998; Becker et al., 2004; Davis et al., 2004] find further evidence of significant flow and circulation through Layer 1 and to a lesser extent in Layer 2 (up to 2 km depth). Models for thermal flow rates support the existence of sub-horizontal conduits in the sheeted dykes that permit substantial lateral transport of fluids. The difference of flow rates measured for Layer 1 and 2 (e.g. 0.1 m/yr versus 0.01 m/yr [Davis et al., 2004]) suggest that flow is essentially decoupled between layers, and that sub-vertical faults (e.g. normal faults at the spreading margin) act as important conduits between them.

Below the dike/gabbro transition the properties of oceanic crust are controlled by bulk composition (as opposed to large fracture networks), imply-

ing that it is impermeable. Together with the absence of K-bearing clays outside anomalous regions such as fractures, it follows that sea water effectively penetrates no deeper than the dike/gabbro transition and is limited to the upper layers of the crust [Salisbury et al.,1989].

These observations lead us to an interpretation of the combined LVZ+LOC layers as oceanic crust that embodies the following elements: **(i)** at or immediately following formation, oceanic crust is intensely hydrated through to the top of layered gabbros near 3.5 km depth, where water is bound within hydrous minerals as temperatures/pressures permit [Rohr, 1994], **(ii)** this structure is preserved with seafloor spreading and ocean basin evolution, until **(iii)** subduction initiates, causing the plate to warm and metamorphic dehydration reactions to occur. These dehydration reactions are largely confined to Layers 1 and 2 (i.e. the LVZ), producing fluids at lithostatic fluid pressures [Fyfe et al., 1978, Christensen, 1984] and resulting in high V_P/V_S values that are maintained by an effectively impermeable plate boundary above, and the gabbroic Layer 3 (i.e. LOC) below. The seismic contrast at the base of the LOC is the oceanic Moho and is defined on compositional grounds. A schematic illustration of the hydrologic cycle of oceanic crust in Cascadia is shown in figure 5.2 that also incorporates elements of previous work by Bostock et al. [2002] and Audet et al. [2009].

This interpretation harbors a number of important implications. We begin by noting that it does not affect earlier conclusions regarding the position of the plate boundary [Audet et al, 2010] nor estimates of permeability and porosity within the LVZ (now, interpreted as the upper portion of oceanic crust) [Peacock et al., 2011]. It is worth recalling that a multi-layered structure associated with the LVZ (or E-layer) has been previously suggested/interpreted on several occasions. Cassidy and Ellis [1993] iden-

tified a weakly contrasting layer below the LVZ within the Juan de Fuca crust, with a combined thickness of 18 – 21 km from analysis of 3 stations on central Vancouver Island, Georgia Strait and mainland British Columbia. These authors employed only forward scattered conversions and so could not resolve the tradeoff between layer thicknesses and interval V_P/V_S , which in the case of the latter quantity we now know to be extreme.

In an analysis of data from Puget Sound, Abers et al. [2009] have also suggested that the LVZ is associated with a 2-layer structure comparable to that presented here, where they refer to the top layer as a low-velocity channel possibly representing metamorphosed subducted sediment. Although we acknowledge that sediments may contribute to the expression of the LVZ, we believe that the structure is fundamentally defined by the distinct porosity/hydration states represented by the basalts/sheeted dykes within Layer 2, and the coarse grained, layered gabbros and cumulates of Layer 3. As mentioned above, these contrasting physical states are clearly evident in exposed (Bay of Islands, Semail) and drilled (Troodos) ophiolites with depth extents that compare favorably with the values of the H_{LVZ} and H_{LOC} estimated here. Note also that our V_P/V_S estimates for the LOC ($R_{LOC} = 1.85 \pm 0.22$) falls comfortably within the range of 1.81-1.94 measured for gabbro in laboratory studies [Christensen, 1996; Salisbury and Christensen, 1978]. This correspondence holds not only across the entire Cascadia margin but also within the 4 individual margin segments.

An important factor working against sediments as the primary component of the LVZ is the ubiquity of LVZs in subduction zones worldwide. For example, a very similar 2-layer structure has been characterized in the southern Mexican subduction zone [Song and Kim, in review]). In Mexico, the sedimentary budget of the incoming plate is only 20% that of Cascadia

(97×10^{12} g/yr terrigenous flux versus 18×10^{12} g/yr [Rea and Ruff, 1996]), rendering it unlikely that sediments play a defining role in generation of the LVZ. Moreover, many other examples exist of LVZs in different subduction zones identified using receiver functions [Yuan et al., 1999, 2000; Bock et al., 2000; Ferris et al., 2003; Kawakatsu and Watada, 2007; Suckale et al., 2009; Kato et al., 2010; Kim et al., 2010; MacKenzie et al., 2010] and guided waves [Abers, 2000; 2005]. Although detailed V_P/V_S ratios have not been measured in most instances, thickness estimates from guided waves again average thinner than typical oceanic crust (1-7 km [Abers, 2000]; 2-8 km [Abers, 2005]). Given their ubiquity, it would appear likely that LVZs share a common origin in most, if not all, instances. This assertion is supported by the observation that the depths at which LVZ signatures disappear in various subduction zones (starting from ~ 45 km in Cascadia to ~ 120 km in Alaska, northeast Japan and the central Andes) invariably match those predicted from thermo-petrological modelling for the onset of the basalt to eclogite transformation (e.g. Peacock and Wang [1999], Rondenay et al. [2008]), and so is consistent with the structural interpretation advanced in this study. Interpretation of the LVZ as underplated sediments, as in e.g. Calvert et al. [2011], is incompatible with this latter observation.

Song and Kim [in review] have recently proposed a mechanism for the development of hexagonal anisotropy within the LVZ of the southern Mexican subduction zone along the MASE experiment profile [Kim et al., 2010]. They modeled received function responses with P -wave and S -wave anisotropies of 10-15%, and fast symmetry axis dipping 10° more steeply than the plate boundary in a direction subparallel to plate motion (ψ). They argue that anisotropy develops as a consequence of crystallographic and shape preferred orientation along foliation planes in response to homogeneous deformation in

a predominantly ductile regime. Anisotropy measurements across southern Vancouver Island (SVI), where data quality is highest, are broadly consistent with the results of Song and Kim [in review]. Our results show magnitudes of P and S anisotropy (9% and 15%, respectively) and a fast symmetry axis generally oriented in downdip direction of subduction, with an average angle of 24° degrees to the plate boundary. Results at other stations in our data set, where data quantity and quality are poorer, proved, however, far more erratic and further analysis of improved data sets will be necessary to fully investigate the relation between anisotropy and deformation in the LVZ.

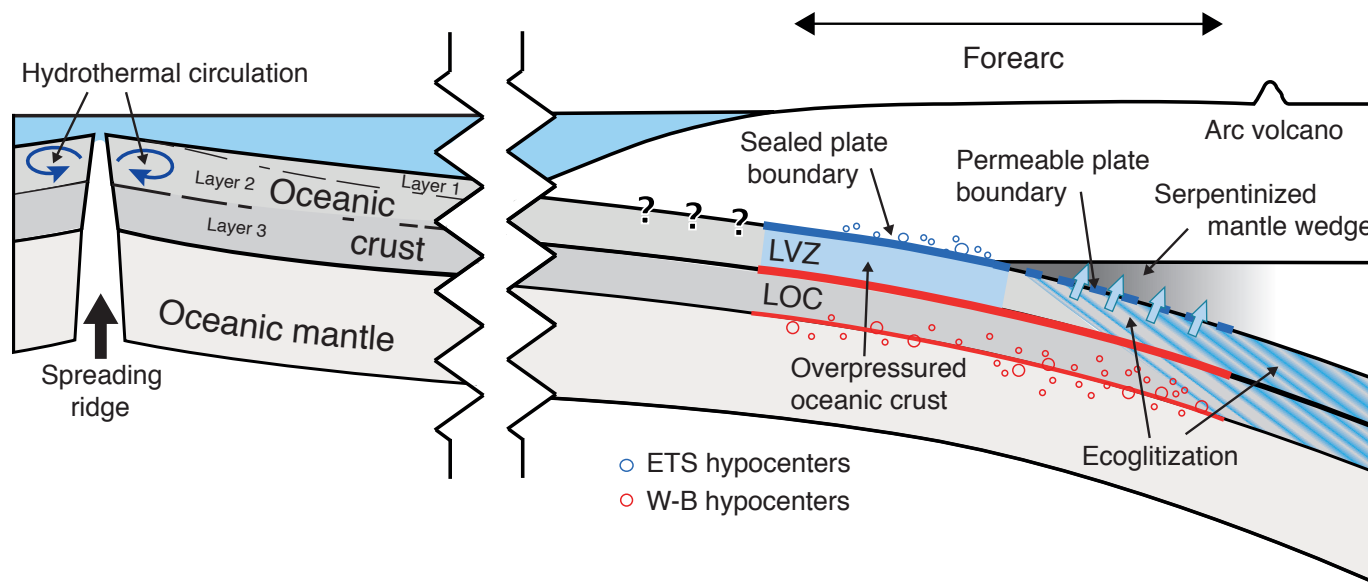


Figure 5.2: Schematic model illustrating hydrologic evolution of oceanic crust in Cascadia from left to right (modified after Audet et al. [2009]). Vigorous hydrothermal circulation near oceanic ridge results in pervasive hydration, preserved as hydrous minerals, in a porous Layer 2. Upon initiation of subduction, metamorphic dehydration reactions (\pm compaction) commences to produce free fluids at near-lithostatic pressures within Layer 2 (\pm Layer 1). Pressure is maintained by an impermeable plate boundary above, and a nonporous Layer 3 (LOC) below, resulting in high V_P/V_S for the LVZ. Eclogitization commences near 45 km depth and is accompanied by a $\sim 10\%$ volume change that compromises the plate boundary seal and initiates serpentization of the mantle wedge. A top to down loss of the LVZ then occurs with increasing depth.

Chapter 6

Conclusions

Receiver function waveform inversion has been employed to compile seismic attributes for the continental crust, and planar dipping layers LVZ and LOC, along the entire Cascadia subduction zone forearc. Depths to the top of the LVZ are comparable to those obtained with a phase stacking approach by Audet et al. [2010] and result in a focussed distribution of ETS locations centered near 30 km depth. The only seismic attribute that exhibits some correlation with segmentation of ETS occurrence intervals/timing as documented by Brudzinski and Allen [2007], is V_P/V_S of overriding continental crust.

We have extended the observations of high V_P/V_S in the LVZ below Vancouver Island [Audet et al., 2010] to the entire Cascadia margin, and the waveform modelling has permitted identification of a weaker layer immediately below. This identification has led to a revised interpretation of the LVZ as the upper portion of the downgoing plate, comprising sediments (Layer 1), and pillow basalts and sheeted dykes (Layer 2). Layer LOC is assigned to the remaining gabbro and ultra-mafics (Layer 3). The new interpretation does not affect previous conclusions regarding position of the plate boundary, nor estimates of permeability and porosity, and is supported by previous studies of ophiolites and *in situ* seismic and hydrological investigations of oceanic crust.

Anisotropic measurements for southern Vancouver Island are comparable to a recent study in southern Mexico [Song and Kim, in review], though a greater variability in observations from other areas along Cascadia invites a future receiver functions investigation of higher quantity and quality data.

References

- Abers, G. A. (2000), Hydrated subducted oceanic crust at 100-250 km depth, *Earth Plan. Sci. Let.*, *176*, 323–330.
- Abers, G. A. (2005), Seismic low-velocity layer at the top of subducting slabs: observations, predictions, and systematics, *Phys. Earth Plan. Int.*, *149*, 7–29, doi:10.1016/j.pepi.2004.10.002
- Abers, G. A., L. S. MacKenzie, S. Rondenay, Z. Zhang, A. G. Wech, and K. C. Creager (2009), Imaging the source region of Cascadia tremor and intermediate–depth earthquakes, *Geology*, *37*, 1119–1122, doi:10.1130/G30143A.1
- Anderson, D. L. (1989), Theory of the Earth, *Blackwell Sci., Malden, Mass.*, 366 pp.
- Audet, P., M. G. Bostock, J. -P. Mercier, and J. F. Cassidy (2008), Morphology of the Explorer-Juan de Fuca slab edge in northern Cascadia: Imaging plate capture at a ridge-trench-transform triple junction, *Geology*, *36*, 895–898.
- Audet, P., M. G. Bostock, N. I. Christensen, and S. M. Peacock (2009),

References

Seismic evidence for overpressured subducted oceanic crust and megathrust fault sealing, *Nature*, 457, 76–78, doi:10.1038/nature07650.

Audet, P., M. G. Bostock, D. C. Boyarko, M. R. Brudzinski, and R. M. Allen (2010), Slab morphology in the Cascadia fore arc and its relation to episodic tremor and slip, *J. Geophys. Res.*, 115, B00A16, doi:10.1029/2008JB006053.

Becker, K., E. E. Davis, F. N. Spiess, and C. P. deMoustier (2004), Temperature and video logs from the upper oceanic crust, holes 504B and 896A, Costa Rica Rift flank: Implications for the permeability of upper oceanic crust, *Earth Planet. Sci. Lett.*, 222, 881–896.

Bock, G., B. Schurr, and G. Asch (2000), High-resolution image of the oceanic Moho in the subducting Nazca plate from P-S converted waves, *Geophys. Res. Lett.*, 27, 3929–3932.

Bostock, M. G., and J. C. VanDecar (1995), Upper mantle structure of the northern Cascadia subduction zone, *Can. J. Earth Sci.*, 32, 1–12.

Bostock, M. G. (1998), Mantle stratigraphy and evolution of the Slave province, *J. geophys. Res.*, 103, 21183–21200.

Bostock, M. G., S. Rondenay, and J. Shragge (2001), Multiparameter two-dimensional inversion of scattered teleseismic body waves : 1 - Theory for oblique incidence, *J. Geophys. Res.*, 106, 3071–30782.

Bostock, M. G., R. D. Hyndman, S. Rondenay, and S. M. Peacock (2002),

References

An inverted continental Moho and serpentinization of the forearc mantle, *Nature*, *417*, 536–538.

Brudzinski, M. R., and R. M. Allen (2007), Segmentation in episodic tremor and slip all along Cascadia, *Geology*, *35*, 907–910.

Burdick, S., C. Li, V. Martynov, T. Cox, J. Eakins, T. Mulder, L. Astiz, F. L. Vernon, G. L. Pavlis, and R. D. van der Hilst (2008), Upper mantle heterogeneity beneath North America from travel time tomography with global and US–Array transportable array data, *Seis. Res. Lett.*, *79*, 384–392.

Calvert, A. J., and R. M. Clowes (1990), Deep, high amplitude reflections from a major shear zone above the Juan de Fuca plate, *Geology*, *18*, 1091–1094.

Calvert, A. J., K. Ramachandran, H. Kao, and M. A. Fisher (2006), Local thickening of the Cascadia forearc crust and the origin of seismic reflectors in the uppermost mantle, *Tectonophysics*, *420*, 175–188.

Calvert, A. J., L. A. Preston, and A. M. Farahbod (2011), Sedimentary underplating at the Cascadia mantle-wedge corner revealed by seismic imaging, *Nature*, *4*, 545–548, doi:10.1038/NGEO1195 .

Cassidy, J. F., and R. M. Ellis (1993), S wave velocity structure of the northern Cascadia subduction zone, *J. Geophys. Res.*, *98*, 4407–4421.

Christensen, N. I. (1984), Pore pressure and oceanic crustal seismic struc-

References

ture, *Geophys. J. R. astr. Soc.*, *79*, 411–423.

Christensen, N. I. (1996), Poisson’s ratio and crustal seismology, *J. Geophys. Res.*, *101*, 3139–3156.

Clowes, R. M., Yorath, C. J., and R. D. Hyndman (1987), Reflection mapping across the convergent margin of western Canada, *Royal Astronomical Society Geophysical Journal*, *89*, 79–84.

Davis, E. E., K. Becker, and J. He (2004), Costa Rica Rift revisited: Constraints on shallow and deep hydrothermal circulation in young oceanic crust, *Earth Planet. Sci. Lett.*, *222*, 863– 879.

DeMets, C., R. G. Gordon, D. F. Argus, and S. Stein (1990), Current plate motions, *Geophys. J. Int.*, *101*, 425–427.

Ferris, A., G. A. Abers, D. H. Christensen, and E. Veenstra (2003), High resolution image of the subducted Pacific (?) plate beneath central Alaska, 50–150 km depth, *Earth Plan. Sci. Lett.*, *214*, 575–588, doi:10.1016/S0012-821x(03)00403-5.

Fisher, A. T., K. Becker, and E. E. Davis (1997), The permeability of young oceanic crust east of Juan de Fuca Ridge determined using borehole thermal measurements , *Geophys. Res. Lett.*, *24*, 1311–1314.

Fisher, A. T. (1998), permeability within basaltic oceanic crust, *Review of Geophysics*, *36*, 143–182.

References

Frederiksen, A. W., and M. G. Bostock (2000), Modelling teleseismic waves in dipping anisotropic structures, *Geophys. J. Int.*, *141*, 401–412.

Frederiksen, A. W., H. Folsom, and G. Zandt (2003), Neighbourhood inversion of teleseismic Ps conversions for anisotropy and layer dip, *Geophys. J. Int.*, *155*(1), 200–212.

Fuis, G. S., J. J. Zucca, W. D. Mooney, and B. Milkereit (1987), A geologic interpretation of seismic refraction results in north-east California, *Geological Society of America Bulletin*, *98*, 53–65.

Fyfe, W. S., N. J. Price, and A. B. Thompson (1978), Fluids in the earth's crust, *Elsevier, New York*, 333pp.

Green, A. G., R. M. Clowes, C. J. Yorath, C. Spencer, E. R. Kanasevich, M. T. Brandon, and B. Sutherland (1986), Seismic reflection imaging of the Juan de Fuca plate, *Nature*, *319*, 210–213.

Hyndman, R. D., and S. M. Peacock (2003), Serpentinization of the forearc mantle, *Earth Planet. Sci. Lett.*, *212*, 417–432.

Kao, H., S.-J. Shan, H. Dragert, G. Rogers, J. F. Cassidy, and K. Ramachandran (2005), A wide depth distribution of seismic tremors along the northern Cascadia margin, *Nature*, *436*, 841–844, doi:10.1038/nature03903.

Kao, H., S.-J. Shan, H. Dragert, and G. Rogers (2009), Northern Cascadia

References

episodic tremor and slip: A decade of tremor observations from 1997 to 2007, *J. Geophys. Res.*, *114*, B00A12, doi:10.1029/2008JB006046.

Kato, A., T. Iidaka, R. Ikuta, Y. Yoshida, K. Katsumata, T. Iwasaki, S. Sakai, C. Thurber, N. Tsumura, K. Yamaoka, T. Watanabe, T. Kunitomo, F. Yamazaki, M. Okubo, S. Suzuki, and N. Hirata (2010), Variations of fluid pressure within the subducting oceanic crust and slow earthquakes, *Geophys. Res. Lett.*, *37*, L14310, doi:10.1029/2010GL043723.

Kim, Y., R. W. Clayton, and J. M. Jackson (2010), Geometry and seismic properties of the subducting Cocos plate in central Mexico, *J. Geophys. Res.*, *115*, doi:10.1029/2009JB006942.

Kawakatsu, H., and S. Watada (2007), Seismic evidence for deep-water transportation in the mantle, *Science*, *316*, 1468–1471.

Kurtz, R. D., J. M. DeLaurier, and J. C. Gupta (1990), The electrical conductivity distribution beneath Vancouver Island: a region of active plate subduction, *J. Geophys. Res.*, *95*, 10929–10946.

Langston, C.A. (1977) Corvallis, Oregon, crustal and upper mantle receiver structure from teleseismic P and S waves. *Bull. Seis. Soc. Am.*, *67*, 713–724.

Langston, C. A. (1981), Evidence for the subducting lithosphere under southern Vancouver island and western Oregon from teleseismic P wave conversion, *J. Geophys. Res.*, *86*, 3857–3866.

References

Ludwin, R. S., C. S. Weaver, and R. S. Crosson (1991), in Neotectonics of North America, D. B. Slemmons, E. R. Engdahl, M. D. Zoback, D. D. Blackwell, *Eds. (Geological Society of America, Boulder, CO, 1991), Decade Map, vol. 1*, pp77–97.

MacKenzie, L. S., G. A. Abers, S. Rondenay, and K. M. Fischer (2010), Imaging a steeply dipping subducting slab in Southern Central America, *Earth Planet. Sci. Lett.*, *296*, 459–468.

Mazzotti, S., H. Dragert, J. Henton, M. Schmidt, R. Hyndman, T. James, Y. Lu, and M. Craymer (2003), Current tectonics of northern Cascadia from a decade of GPS measurements, *J. Geophys. Res.*, *108*, B12, 2554, doi:10.1029/2003JB002653.

McCrorry, P. A., J. L. Blair, and D. H. Oppenheimer (2006), Depth to the Juan de Fuca slab beneath the Cascadia subduction margin - A 3-D model for sorting earthquakes, *U.S. Geol. Surv. Data Ser.*, *91*, U.S. Geol. Surv., Reston, Va. (Available at <http://pubs.usgs.gov/ds/91/>).

Mercier, J. -P., M. G. Bostock, J. F. Cassidy, K. Dueker, J. B. Gaherty, E. J. Garnero, J. Revenaugh, and G. Zandt (2009), Body wave tomography of western Canada, *Tectonophysics*, *475*, 480–492.

Michaelson, C. A., and C. S. Weaver (1986), Upper mantle structure from teleseismic P wave arrivals in Washington and Northern Oregon, *J. Geophys. Res.*, *91*, 2077–2094.

References

Muller, J. E. (1977), Evolution of the Pacific Margin, Vancouver Island and adjacent regions, *Canadian Journal of Earth Sciences*, *14*, 2062–2084, 10.1139/e77-176.

Nabelek, J., X. -Q. Li, S. Azevedo, J. Braunmiller, A. Fabritius, B. Leitner, A. Trehu, and G. Zandt (1993), A high-resolution image of the Cascadia subduction zone from teleseismic converted phases recorded by a broadband seismic array, *Eos Trans. AGU*, *74*(43), Fall Meet. Suppl., 431.

Nicholson, T., M. G. Bostock, and J. F. Cassidy (2005), New constraints on subduction zone structure in northern Cascadia, *Geophys. J. int.*, *161*, 849–859.

Obrebski, M., R. M. Allen, M. Xue, and S. -H. Hung (2010), Slab-plume interaction beneath the Pacific Northwest, *Geophys. Res. Lett.*, *37*, L14305, doi:10.1029/2010GL043489.

Oldow, J. S., A. W. Bally, H. G. Avé Lallemant, and W. P. Leeman (1989), Phanerozoic evolution of North American Cordillera; United States and Canada, in: *The geology of North America - An Overview*, 139-232.

Peacock, S. M., and K. Wang (1999), Seismic consequences of warm versus cool subduction metamorphism: Examples from southwest and northeast Japan, *Science*, *286*, 937–939.

Peacock, S. M., N. I. Christensen, M. G. Bostock, and P. Audet (2011), High pore pressures and porosity at 35 km depth in the Cascadia subduc-

References

tion zone, *Geology*, *39*, 471–474, doi:10.1130/G31649.1.

Ramachandran, K., S. E. Dosso, G. D. Spence, R. D. Hyndman, and T. M. Brocher (2005), Forearc structure beneath southwestern British Columbia: A three-dimensional tomographic velocity model, *J. Geophys. Res.*, *110*, B02303, doi:10.1029/2004JB003258.

Rasmussen J., and E. Humphreys (1988), Tomography image of the Juan de Fuca plate beneath Washington and western Oregon using teleseismic P-wave travel times, *Geophys. Res. Lett.*, *15*, 1417–1420.

Rea, D. K., and L. J. Ruff (1996), Composition and mass flux of sediment entering the world's subduction zones: Implications for global sediment budgets, great earthquakes, and volcanism, *Earth Planet. Sci. Lett.*, *140*, 1–12.

Rogers, G., and H. Dragert (2003), Episodic Tremor and Slip on the Cascadia subduction zone: The chatter of silent slip, *Science*, *300*, 1942–1943.

Rohr, K. M. M. (1994) Increase of seismic velocities in upper oceanic crust and hydrothermal circulation in the Juan de Fuca plate, *Geophys. Res. Lett.*, *21*, 2163–2166.

Rondenay, S., M. G. Bostock, and J. Shragge (2001), Multiparameter two-dimensional inversion of scattered teleseismic body waves: 3 - Application to the Cascadia 1993 data set, *J. Geophys. Res.*, *106*, 30795–30807.

Rondenay, S., G. A. Abers., and P. E. van Keken (2008), Seismic imaging of

References

subduction zone metamorphism, *Geology* 36, 275–278, doi: 10.1130/G24112A.1.

Salisbury, M.H., and N. I. Christensen (1978), The seismic velocity structure of a traverse through the Bay of Islands ophiolite complex, Newfoundland, an exposure of oceanic crust und upper mantle, *J. Geophys. Res.*, 83, 805–817.

Salisbury, M. H., N. I. Christensen, F. J. Vine, G. C. Smith, and S. Eleftheriou (1989), Geophysical structure of the Troodos ophiolite from downhole logging, *Cyprus crustal study project: initial report*, hole CY-4, 331–350.

Sambridge, M. (1999), Geophysical inversion with a neighbourhood algorithmI. Searching a parameter space, *Geophys. J. Int.*, 138, 479–494.

Smith, S. W., and J. S. Knapp (1993), Seismicity of the Gorda Plate, Structure of the Continental Margin, and an Eastward Jump of the Mendocino Triple Junction, *J. Geophys. Res.*, 98, 8152–8171.

Song, T. -R. A, and Y. Kim (in review), Localized seismic anisotropy associated with slow earthquakes beneath southern Mexico, *submitted for review*, 2011.

Soyer, W., and M. Unsworth (2006), Deep electrical structure of the northern Cascadia (British Columbia, Canada) subduction zone: Implications for the distribution of fluids, *Geology*, 34, 53–56; doi: 10.1130/G21951.1.

Suckale, J., S. Rondenay, M. Sachpazi, M. Charalampakis, A. Hosa, and L.

References

H. Royden (2009), High-resolution seismic imaging of the western Hellenic subduction zone using teleseismic scattered waves, *Geophys. J. Int.*, *178*, 775–791, doi: 10.1111/j.1365-246X.2009.04170.x.

Trehu, A. M., I. Asudeh, T. M. Brocher, J. H. Luetgert, W. D. Mooney, J. L. Nabelek, and Y. Nakamura (1994), Crustal architecture of the Cascadia fore-arc, *Science*, *266*, pp 237–243, doi:10.1126/science.266.5183.237.

Wada, I., and K. Wang (2009), Common depth of slab-mantle decoupling: Reconciling diversity and uniformity of subduction zones, *Geochem. Geophys. Geosyst.*, *10*, Q10009, doi:10.1029/2009GC002570.

Wagner, L., D. W. Forsyth, M. J. Fouch, and D. E. James (2010), Detailed three-dimensional shear wave velocity structure of the northwestern United States from Rayleigh wave tomography, *Earth Planet. Sci. Lett.*, *299*, 273–284.

Wech, A.G. (2010), Interactive Tremor Monitoring, *Seismol. Res. Lett.*, *81*, 4.

Wessel, P., and W. H. F. Smith (1991), Free software helps map and display data, *Eos Trans. AGU*, *72*, 441.

Xue, M., and R. M. Allen (2007), The fate of the Juan de Fuca plate: Implications for a Yellowstone plume head, *Earth Planet. Sci. Lett.*, *264*, 266–276.

References

Xue, M., and R. M. Allen (2010), Mantle structure beneath the western United States and its implications for convection processes, *J. Geophys. Res.*, *115*, B07303, doi:10.1029/2008JB006079.

Yuan, H., J. Park, and V. Levin (1999), P-to-S converted phases from subducted slabs in the northwest Pacific, *Eos Trans. AGU*, *80*, Fall Meet. Suppl., F720.

Yuan, X., S. V. Sobolev, R. Kind, O. Oncken, G. Bock, G. Asch, B. Schurr, F. Graeber, A. Rudloff, W. Hanka, K. Wylegalla, R. Tibi, C. Haberland, A. Rietbock, P. Giese, P. Wigger, P. Röwer, G. Zandt, S. Beck, T. Wallace, M. Pardo, and D. Comte (2000), Subduction and collision processes in the central Andes constrained by converted seismic phases, *Nature*, *408*, 958–961.

Zhu, L., and H. Kanamori (2000) Moho depth variation in southern California from teleseismic receiver functions. *J. Geophys. Res.*, *105*, 2969–2980.